Composite Structures 375 (2026) 119787

Contents lists available at ScienceDirect

Composite Structures

journal homepage: www.elsevier.com/locate/compstruct

Exploiting the self-sensing capabilities of buckypapers for in-situ monitoring of impacts and compression after impact on GFRP panels

Lucio Pinello *, Patel Bhavik, Marco Giglio, Claudio Sbarufatti

Department of Mechanical Engineering - Politecnico di Milano, Via La Masa 1, Milano, 20156, Italy

ARTICLE INFO

Keywords:
CNT
Buckypapers
SHM

ABSTRACT

This paper delves into the application of buckypaper (BP) in enhancing the development of multifunctional Glass-Fibre Reinforced Polymers (GFRPs) integrated with carbon nanotubes (CNTs) for use in Structural Health Monitoring (SHM) applications. The growing demand for composite materials, driven by their outstanding mechanical properties and cost-effectiveness, has spurred the search for innovative damage-sensing techniques. In this context, CNT-based nanocomposites have emerged as a promising alternative due to their piezoresistive properties, providing real-time deformation and damage monitoring capabilities. This study investigates the fabrication and performance of CNT-doped GFRP materials featuring varying CNT concentrations. Tensile tests confirm that BP integration does not compromise mechanical strength, with the resultant sensing network demonstrating heightened sensitivity to strain and early damage detection capabilities. Low-Velocity Impact (LVI) tests show CNTs' ability to detect dynamic events, characterised by distinct resistance variations linked to impact-induced damage. Compression After Impact (CAI) tests provide additional evidence of BP's potential for damage detection, highlighting resistance variations associated with compression, buckling and complete specimen failure. These findings highlight the potential of buckypaper-based CNT composites for in-situ SHM applications. The ease of application, absence of CNT agglomeration and minimal impact on host material properties make BP an appealing choice for various industrial applications.

1. Introduction

According to a recent market study, the global impact of Fibre Reinforced Polymer (FRP) is projected to grow by 4.3% [1]. This surge in demand for lightweight composite materials is attributed to several factors, including their exceptional mechanical properties, resistance to fatigue and corrosion, and competitive cost compared to conventional industrial metal alloys. Several non-destructive techniques, such as strain gauges and optical fibres, have been widely employed to monitor the behaviour and damage of FRPs. While effective, these approaches are typically local or directional in nature and thus may not provide a comprehensive picture of damage evolution in real-time [2–4]. This limitation has motivated increasing interest in multifunctional composites with embedded self-sensing capabilities [5–8]. In this context, Carbon nanotubes (CNT) have emerged as a multifunctional nanofiller for FRPs, forming conductive percolation networks within the polymer matrix. Utilising the piezoresistive properties of CNT, these composites can autonomously detect deformation and damage in real-time, offering a promising alternative to traditional sensing methods. Thanks to the CNT's piezoresistive nature, this is achieved by measuring the electrical resistance of the monitored structure, which is related to the structure's strains. Therefore, these CNT-based nanocomposites aim to replace conventional metal foil-based strain gauges and optical fibres, which have limitations such as a restricted gauge factor, location specificity and an inability to sense transversely grown cracks [9,10]. In addition, CNT dispersion not only improves the electrical properties of the host materials, which makes them suitable as self-sensing materials, but it can also enhance the mechanical properties of the host materials [11–15]. However, the impact on both the electrical and mechanical properties of the host materials depends on the CNT concentration and dispersion. In this regard, numerous CNT architectures and configurations have been investigated, with many demonstrating high stability and piezoresistivity correlated with applied mechanical strains and induced damage [12,16–19]. Several studies have focused on the dispersion technique of CNT within a polymer matrix for nanocomposite fabrication. This method is effective when limited CNT content is required and damage detection needs to be localised. However, achieving a homogeneous distribution of nanoparticles remains challenging, as uneven distribution leads to CNT agglomeration, which can induce failure [20]. Additionally, some studies have reported a reduction in tensile strength when CNT concentration goes beyond a certain limit [13]. Therefore,

* Corresponding author.
E-mail address: lucio.pinello@polimi.it (L. Pinello).

https://doi.org/10.1016/j.compstruct.2025.119787
Received 30 May 2025; Received in revised form 5 September 2025; Accepted 23 October 2025
Available online 27 October 2025

achieving a uniform distribution of nanoparticles is crucial to maximising the potential of these self-sensing composites. Various methods, including mini-calendering, sonication, ultrasonication, and resin treatment, have been proposed to improve dispersion [16,18]. Nevertheless, a unanimous consensus on the most effective approach remains elusive. As a result, it is common practice in monitoring applications to verify the absence of a detrimental effect on the mechanical properties. To address the challenge of non-uniform CNT dispersion and its effect on mechanical properties, researchers have explored the application of thin and porous membranes of highly entangled CNT, known as buckypaper (BP), in the development of self-sensing composites. BP is formed through processes like vacuum filtration or slurry compression, resulting in a mesoporous structure with densely packed, randomly oriented CNT that resist agglomeration [21,22]. Embedding BP sheets within interlaminar regions of composite materials enhances electromechanical performance, allowing strain-related measurements to be taken closer to damage-prone areas [23]. The integration of BP sheets is repeatable and straightforward, creating highly sensitive and reliable sensor networks able to sense strain-related quantities. These BP-based composites are particularly well-suited for Structural Health Monitoring (SHM) applications by relying on electrical resistance variation measurements [24–26]. While the mechanical response of FRPs to low-velocity impact has been extensively studied and is well-documented in the literature [27–29], limited research has specifically addressed the role of buckypapers during LVI events [30]. In particular, the post-impact electro-mechanical behaviour of buckypaper-based sensing layers remains largely unexplored. Therefore, this research integrates buckypapers into Glass- Fibre- Reinforced Plastic (GFRP) panels to investigate (i) the effect of BP on the mechanical properties of the host materials, (ii) BP's ability to exhibit self-sensing properties even in the presence of impact-induced damage, and (iii) how the BP location through the thickness of the panel affects its sensitivity to impact-induced damage. To achieve these aims, GFRP panels were fabricated with three different concentrations of CNT-based buckypapers to compare the effects of different CNT concentrations on both strain and damage sensitivity and host material mechanical properties. Specimens were then cut from the panels for (i) tensile tests and (ii) Low-Velocity Impact (LVI) and Compression After Impact (CAI) tests. Tensile specimens were subjected to longitudinal tensile loading to evaluate the effect of BP on the overall mechanical strength of GFRP composites and to verify the ability of BP-based monitoring to detect damage. Specimens subjected to LVI and CAI tests were fabricated with the BP positioned far from the bending neutral plane to maximise the bending-induced strains experienced by the BP during impacts. The LVI tests were performed by impacting either the surface close to or far from the buckypapers to observe how the through-thickness distance between the impact location and the BP affects sensing capabilities. Finally, impacted specimens were subjected to Compression After Impact (CAI) tests to assess their post-impact damage-sensing capabilities. The paper is structured as follows: Section 2 describes the electric conduction mechanisms involved when dealing with CNT. Section 3 discusses the fabrication of BP composites, the experimental procedure, and the data acquisition systems. Section 4 presents the results of the tensile, LVI, and CAI tests. Finally, the conclusions and discussions on future prospects are presented, providing insights into the interpretation of results and potential applications of self-sensing composites.

2. Buckypaper-based monitoring approach

Buckypapers are thin, porous membranes of highly entangled CNT, as described in Section 1. Specifically, CNT are piezoresistive, meaning that strains are reflected in electrical resistance variations, which can be exploited for SHM purposes to obtain the aforementioned strain-related measurements [24–26].

The piezoresistive behaviour of the CNT is due to three factors: (i) the intrinsic electrical conductivity of carbon nanotubes, (ii) the direct electrical contact between the adjacent nanoparticles, and (iii) the tunnelling effects between neighbouring nanoparticles that are not in contact. The tunnelling effect allows electrons to migrate between two adjacent conductive particles, provided they are within 1.8 nm of each other. An electrical series model has been proposed to model the conductive mechanisms in terms of electrical resistance in a representative cubic volume [31] in which threefold contributions give the electrical resistance:

- The intrinsic electrical resistance of each nanotube, R_{cnt};
- The electrical resistance of the contact between CNT, $R_{contact}$;
- The tunnelling resistance, R_{tun}, which is the electrical resistance associated with the migration of electrons between two adjacent conductive nanoparticles when they are within approximately 1.8 nm of each other (tunnelling effect). This is considered to play a predominant role in the conductivity of percolation paths [31–33].

The intrinsic resistance of CNT depends on: the cross-sectional area A_{cnt} of the nanotube, the intrinsic conductivity σ_{cnt} of the nanoparticle itself, and the length l_{cnt} between the two nearest contact points with the neighbouring CNT, as expressed in Eq. (1).

$$R_{cnt} = \frac{1}{\sigma_{cnt}} \frac{l_{CNT}}{A_{cnt}} \tag{1}$$

The contact resistance is inversely proportional to the number of conducting channels [34] among the nanoparticles in the representative volume, as represented in Eq. (2)

$$R_{contact} = \frac{h}{2e^2} \frac{1}{MT} \tag{2}$$

where M is the number of conducting channels (approximately between 400 and 500 [35]), the ratio h/e^2 is called Planck resistance, and T stands for the transmission probability of electrons tunnelling through the polymer as described in Eq. (3), where d_w is the van der Waals distance, 0.34 nm, m_{cnt} is the mass of the nanotube, and ϕ_{cnt} is the working function of CNT and equal to 4.5 eV.

$$T = e^{-\frac{d_w}{h}/\sqrt{8m_{cnt}\phi_{cnt}}} \tag{3}$$

Ultimately, the mathematical expression of the tunnelling resistance is given by Eq. (4) [33]

$$R_{tunnel} = \frac{V}{A_{tun}J} = \frac{h^2 t_{tun}}{A_{tun}e^2\sqrt{2m_{cnt}\phi}} e^{\frac{4\pi t_{tun}}{h}\sqrt{2m_{cnt}\phi}} \tag{4}$$

where V is the electrical potential difference, J is the tunnelling current density, A_{tun} is the tunnelling area, t_{tun} is the tunnelling distance, and ϕ denotes the height barrier of the insulating resin, which is 0.75 eV [33,36]. According to the above equation, the tunnelling resistance increases exponentially with the tunnelling distance between adjacent nanoparticles, and the material remains electrically conductive when $t_{tun} < 1.8$ nm [32]. The first two contributions, R_{cnt} and $R_{contact}$, act in parallel with respect to the tunnelling resistance because they rely on the contact between nanoparticles, while R_{tun} requires nanoparticles to be within $1.8nm$ of each other to allow electron flow. The total electrical resistance variation can be directly correlated with deformations and damage, such as cracks and delaminations, and induce local distortions in the CNT network, leading to (i) the creation/rupture of contacts between CNT and (ii) changes in the distance between CNT that are not in contact. In both cases, the result is that the conductivity of the CNT network changes. Therefore, this work explores the conductivity of the buckypaper for non-destructive evaluation (NDE) to monitor mechanical loads and assess damage based on the electrical behaviour of the CNT network.

However, it is common practice in the SHM field to use the normalised resistance variation [%] for monitoring purposes [30,37–45]

because it provides information about loads dynamics and their effect on the electromechanical performance of the structure, regardless of the initial resistance value. The normalised resistance variation is defined in Eq. (4), which is derived from the Ohm's law, applying a constant current to the CNT network and measuring the voltage.

$$\Delta R_n = \frac{R(t) - R_0}{R_0} = \frac{V(t) - V_0}{V_0} \tag{5}$$

Eq. (5) calculates the normalised electrical resistance ΔR_n as the difference between the instantaneous electrical resistance $R(t)$ and the initial electrical resistance value R_0, divided by the initial electrical resistance. Then, by applying Ohm's law and considering a constant current, it is possible to express the ΔR_n as a function of the measured voltage $V(t)$ and the initial voltage V_0.

The normalised resistance ΔR_n evaluated according to Eq. (5) will be used in Section 4 to investigate BP's monitoring abilities.

3. Materials and methods

This section outlines the specimens' manufacturing process and the experimental test programme. Section 3.1 focuses on the manufacturing procedure used to create the specimens. Sections 3.2, 3.3, and 3.4 address the experimental setup of tensile tests, LVI impacts, and CAI tests, respectively. Finally, Section 3.5 describes the acquisition system used for collecting electrical measurements for the buckypaper-based monitoring system.

3.1. Specimens manufacturing

Glass Fibre Reinforced Plastic (GFRPs) specimens were fabricated using 16 layers of E-glass woven 0°/90° plies, with an approximate pre-curing thickness of 0.28 mm for each layer. The polymer matrix was a thermoset epoxy resin. Specimen fabrication followed a wet layup procedure. The buckypaper (BP), consisting of highly aligned multi-walled carbon nanotube (MWCNT) sheets, was incorporated as an additional layer positioned between the 14th and 15th ply, with layer counting starting from the bottom, as illustrated in Fig. 1. This position was chosen to maximise strain sensitivity under bending (being farther from the neutral axis), to enable straightforward electrical connections, and to allow the study of the effect of proximity to the impact location by impacting on either the near or far face of the laminate. Furthermore, thin brass squares measuring $5 \times 5 \times 0.015$ mm, coated with silver ink, were affixed to the surface of the buckypaper to facilitate the acquisition of electrical signals. The prepared laminates then underwent curing at 125 °C under 1 bar of pressure for 1 h. The thickness of the composite panels at the end of the curing process was 4.48 mm. Specifically, buckypapers with distinct concentrations of MWCNT were selected and used: 20 gsm (1.9 g of MWCNT), 45 gsm (4.1 g of MWCNT), and 60 gsm (5.42 g of MWCNT), as reported in Table 1. The buckypapers were characterised by highly aligned carbon nanotube sheets with porosities ranging from 80% to 85% and sourced from Nanotech [46]. Two types of BP-GFRP specimens were cut from the composite panels as follows: (i) 150 × 22 mm (length × width) specimens to be used for tensile tests (Type-1 specimens), and (ii) 150 × 100 mm specimens for Low-Velocity Impact and Compression After Impact tests (Type-2 specimens). Two Type-1 specimens were created for each buckypaper surface density and labelled as follows: BP-20-1, BP-20-2, BP-45-1, BP-45-2, BP-60-1, and BP-60-2. Similarly, two Type-2 specimens for each buckypaper surface density are realised (named A and B): BP-20 A, BP-20B, BP-45 A, BP-45B, BP-60 A, and BP-60B. The same procedure was followed without adding buckypapers to realise a neat GFRP plate. Two Neat Type-1 specimens, i.e., Neat −1 and Neat −2, were cut from the latter to observe the influence of BP addition on mechanical strength.

Table 1
Table of BP surface density and MWCNT.

BP surface density [gsm]	20	45	60
MWCNT density [gm]	1.9	4.1	5.42
Nomenclature	BP 20	BP 45	BP 60

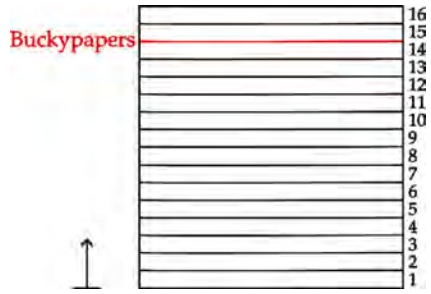

Fig. 1. Stacking sequence and buckypaper placement.

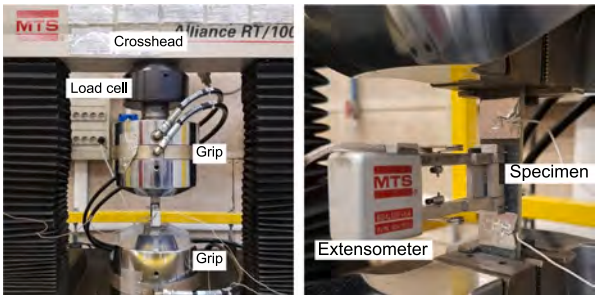

Fig. 2. Experimental test setup used for the tensile test: (a) view of machine crosshead, grips, and load cell, and (b) magnification on extensometer and specimen.

3.2. Tensile tests

Tensile tests were conducted on Type-1 specimens following ASTM D3039 [47], both with and without buckypapers, to assess the effect of the added buckypaper on the mechanical strength. The MTS Alliance RT 100 testing machine was used in displacement control. The crosshead speed was set to 1 mm/min, a value lower than the commonly employed 2 mm/min, to enhance the stability of electromechanical data acquisition. This choice does not influence the mechanical response of the specimens, as the test remains quasistatic, but only increases the total time to failure. Force and displacement data were recorded at a sampling rate of 10 Hz. Additionally, the longitudinal strain was monitored with the same sampling frequency using an MTS 634.12 F-54 extensometer with a 25 mm gauge length. A mechanical gripping system was used to apply a pressure of 7 MPa, preventing any slippage between the grip face and test coupons. Fig. 2 shows the experimental setup used.

3.3. Low-velocity impact tests

Low-Velocity Impact (LVI) tests were conducted on Type-2 specimens using a drop tower and an impactor, according to the ASTM D7136 standard [48]. The impactor was equipped with a Kistler Quartz Force Link type 9331B load cell with a range of ±20 kN, enabling the recording of the load history during the tests. To prevent electrical contact between the impactor and the specimens, a 16 mm hemispherical steel tip with a Teflon adaptor was used as shown in Fig. 3(a). The specimens were clamped to the ground using a fixture

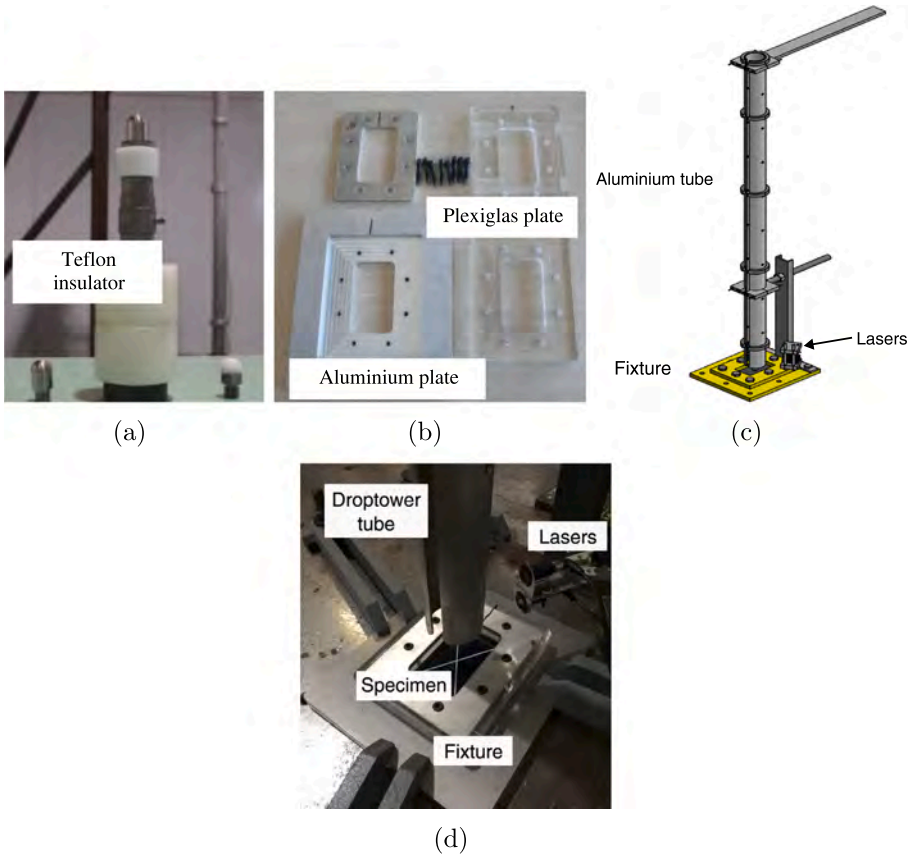

Fig. 3. Impact test configuration: (a) impactor with Teflon insulator, (b) aluminium and plexiglass fixtures, (c) experimental setup, and (d) drop tower apparatus.

made of plexiglass and aluminium plates to ensure proper electrical insulation, as shown in Fig. 3(b). The impact velocity, i.e., the energy, was measured by using two Mikroelektronik M5L/20 lasers placed at 41 mm apart, recording the time it took for the impactor to cross the lasers. Figs. 3(c) and 3(d) show the experimental setup and the placement of the two lasers at the end of the aluminium tube. The drop tower apparatus consists of an aluminium tube that guides the impactor towards the sample. The aluminium tube, depicted in Fig. 3(d), has a length of 1.55 m and an external diameter of 75 mm and a thickness of 4 mm. Holes were drilled along the tube to prevent any possible effects from compressed air during the fall. A clearance of 1 mm was maintained along the length of the tube. An electromagnet was used to hold the impactor at the desired height and release the impactor onto the specimen once deactivated. Rebounds were prevented by sliding an aluminium plate over the sample fixture, as allowed by the standard [48]. The specimens were impacted with 30.41 J of energy during the LVI tests. With the frictional effects between the air and the impactor considered negligible, a total mass of 2 kg was used to achieve the desired impact energy. The tests were performed by impacting either the surface close to or far from the buckypapers to observe the effect of the through-thickness distance between the impact location and the BP on the sensing capabilities. This is done because, depending on the impact location, the buckypapers could experience either tensile or compressive strains, as shown in Fig. 4. Specifically, the specimens labelled 20A, 45A, and 60A were impacted on the rear side, while specimens 20B, 45B, and 60B were impacted on the front side, as detailed in Table 2. The terms "front side" and "rear side" refer, respectively, to the face closer to the buckypapers, i.e., the upper free surface of the 16th layer in Fig. 1, and the face far from the buckypapers, i.e., the lower free surface of the 1st layer in Fig. 1.

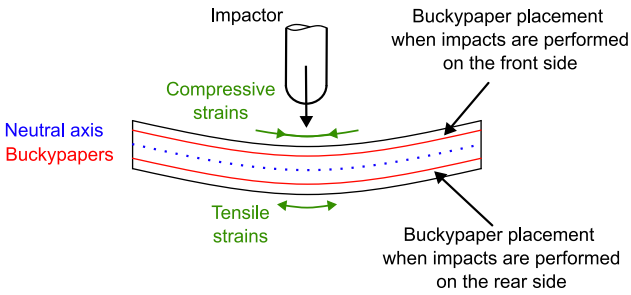

Fig. 4. Schematics of the strains to which the buckypaper is subjected depending on the impacted surface.

Table 2
Test plan for LVI impact tests.

Specimen name	Impact side	Impact energy [J]
BP-20-A	Rear	30.41
BP-20-B	Front	30.41
BP-45-A	Rear	30.41
BP-45-B	Front	30.41
BP-60-A	Rear	30.41
BP-60-B	Front	30.41

3.4. Compression after impact tests

Compression After Impact (CAI) tests were conducted on Type-2 specimens following the ASTM D7137 standard [49]. The testing machine used was the MTS Alliance RT 150 equipped with a 150 kN load cell. The test was conducted in displacement control with a 1.25

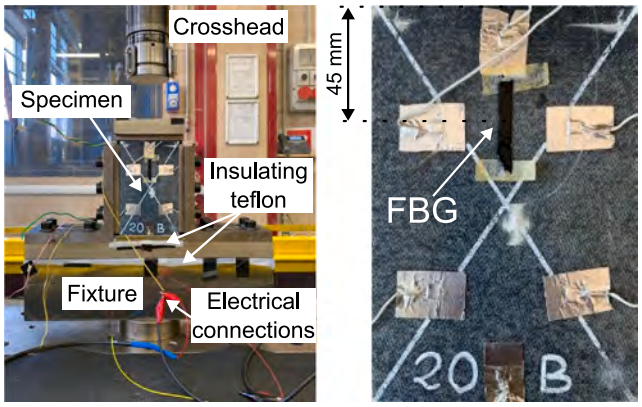

Fig. 5. Compression After Impact test (a) setup, and (b) representative specimen with the FBG strain sensor location highlighted.

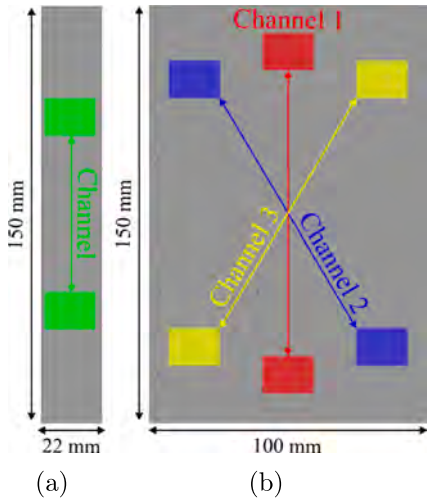

Fig. 6. Schematics of the electrical channels for (a) Type-1 and (b) Type-2 specimens.

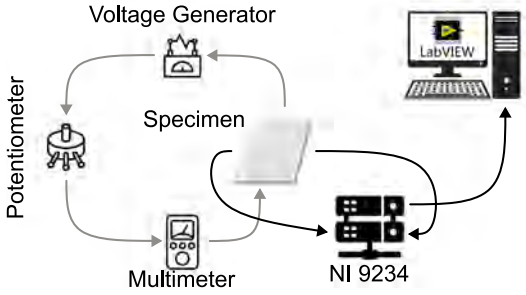

Fig. 7. Data acquisition system, where the grey line represents the electrical circuit used to acquire measurements, and the black line represents the data acquisition path.

mm/min crosshead speed until failure. Both the load and displacement were recorded during the test. The experimental setup used is depicted in Fig. 5a. Since the setup was made of steel, which is electrically conductive, Teflon films were added between the specimens and the CAI fixture to ensure electrical insulation. The samples were simply supported by the lower compression plate, while the compressive load was applied by the upper compression plate under the displacement of the crosshead. A clearance of 1 mm was ensured between the angle plates and the specimens to allow the lateral expansion of the latter during the compression. The ASTM standard recommends using two strain gages at the top of the sample to verify if the applied compressive load is longitudinal and to identify plate instability due to global buckling. In this work, a Fiber Bragg Grating (FBG) sensor with a nominal wavelength of 1530 nm was positioned on the impacted surface for the same purpose. It was placed 45 mm from the top of the specimens along their vertical axis of symmetry, as schematised in Fig. 5b. An optical interrogator was used to acquire strain data, with the signals recorded at 10 Hz on a computer running the HBM CatmanAP software.

3.5. The electrical measurements acquisition system

This work aims to demonstrate the applicability of buckypapers for SHM purposes. Therefore, electrical measurements were acquired to monitor deformation and damage in the buckypapers, as outlined in Section 2. As described by Eq. (5), it is possible to measure the electrical voltage across two points of a buckypaper sheet to monitor the normalised electrical resistance if a constant current passes through the buckypaper. To facilitate this, electrical terminals were created on the sample using brass squares, while thin copper wires and silver ink were used to form electrical channels. A single channel was created for Type-1 specimens, as depicted in Fig. 6a. In contrast, three electrical channels were prepared for Type-2 specimens to monitor a larger area. According to the schematics in Fig. 6b, Channel 1 (represented in red) monitored along the vertical axis of symmetry of the specimens, while Channel 2 and Channel 3 (depicted in blue and yellow, respectively) were used to monitor along the diagonals of the specimens. Ideally, in this way, all the channels monitor the centre of the specimens, i.e., the impact location during the Low-Velocity Impact tests. To enable voltage monitoring, an active potentiometer and a 20.4 V voltage generator were connected in series to continuously supply a 0.39 A current through the BP. The National Instrument 9234 DAQ voltage acquisition system was used to monitor the voltage at 10 kHz. The NI 9234 DAQ voltage acquisition system has a ±5 V range. A LabView code was developed to control the acquisition system and collect data. The acquisition system for normalised electrical resistance variation measurements is schematised in Fig. 7.

4. Results and discussion

This section describes the results from the experimental programme detailed in Section 3. Section 4.1 compares the mechanical strength of specimens with and without the addition of BP and analyses the effect of different BP surface densities on the electrical behaviour of the specimens. This preliminary analysis is crucial for verifying the absence of detrimental effects of the buckypaper addition on the components' mechanical properties and for assessing the ability of the BP-based monitoring system to measure strains and detect damage. Section 4.2 focuses on the LVI impact test, while Section 4.3 discusses the electromechanical properties of the CNT-based sensor network following the impact damage induced during the LVI tests.

4.1. Tensile tests

Tensile tests were conducted to compare the mechanical behaviour of Neat Type-1 specimens with that of Type-1 specimens with the addition of buckypaper and to observe the latter's electromechanical behaviour at varying BP surface densities.

The tensile tests show that the mechanical strength of the GFRP specimens is not affected by the addition of buckypapers, as shown in Fig. 8. Table 3 presents the Ultimate Tensile Stress (UTS) values for each specimen. From these values, it is possible to confirm quantitatively that there is no significant effect of the addition of buckypaper on the specimens' UTS. However, it can be observed from Fig. 8 that there is a slight increase in the elastic modulus of the specimens with

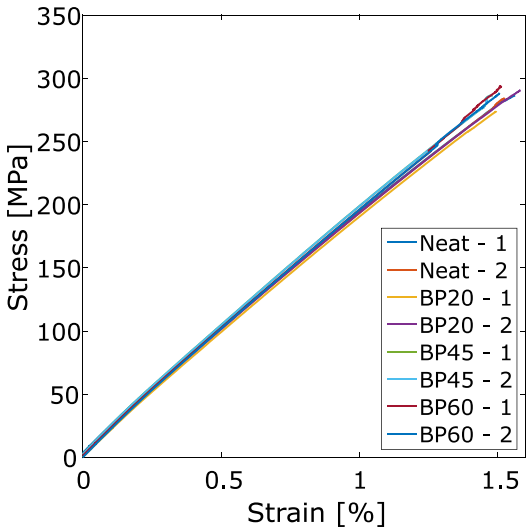

Fig. 8. Tensile test results for Neat Type-1 and Type-1 specimens.

Table 3
Ultimate Tensile Stress (UTS) in MPa for Type-1 specimens.

Specimen	UTS [MPa]
Neat-1	286.45
Neat-2	284.46
BP-20–1	273.93
BP-20–2	290.48
BP-45–1	286.58
BP-45–2	284.48
BP-60–1	293.88
BP-60–2	288.29

buckypaper surface densities of 45 and 60 gsm. This finding is relevant because it shows that buckypapers help mitigate the detrimental effects of increasing CNT concentration in bulk-CNT composites, where higher CNT content may lead to CNT agglomeration, which causes localised stress concentrations, thereby promoting early crack initiation and reducing the nanocomposite's mechanical strength [13,20].

Having confirmed that the addition of buckypaper does not compromise the mechanical properties of components, we can now focus on their applicability for SHM purposes. This involves analysing the electrical response, i.e., the measured normalised resistance ΔR_n, and observing how it is affected by the applied mechanical load. The stress–strain and ΔR_n-strain curves are reported together in the following figures, with the stress–strain curve represented in blue and the ΔR_n-strain curve shown in orange. The analysis is first presented for each individual specimen, followed by general observations. Before proceeding with the analysis of the electromechanical response, it is important to note that buckypapers with different surface densities, i.e., MWCNT content, are used to compare their conductivities and assess how the different conductivities affect the sensing properties, in particular, the electromechanical behaviour. For well-dispersed nanotubes, the higher the MWCNT content, the higher the electrical conductivity of the buckypaper, as can be seen in Section 2. Therefore, the electrical resistance is expected to decrease as the surface density increases from 20 gsm to 60 gsm. This is confirmed in Table 4, which shows the electrical resistance of Type-1 specimens at the beginning of the tensile test. As a result, improved sensing capabilities are expected for specimens with higher conductivity because they will be more sensitive to lower strains and the initiation of damage.

Starting with specimen BP-20-1, Fig. 9a shows the electromechanical signals acquired during the loading and unloading phases of the tensile test. The normalised electrical resistance variation ΔR_n increases

Table 4
Electrical resistance R [Ω] of Type-1 specimens at the beginning of the tensile test.

Specimen	R [Ω]
BP-20–1	7.6874
BP-20–2	8.1706
BP-45–1	4.7575
BP-45–2	4.5222
BP-60–1	2.8080
BP-60–2	2.5726

with the applied load until a significant ΔR_n oscillation is registered at 229.69 MPa (1.49% strain). From this point on, the unloading phase takes place with the specimen being subjected to permanent damage, as shown by the constant ΔR_n value of 112.57%. Focusing on the loading phase, Fig. 9b reveals some interesting features of the normalised electrical resistance variation curve, which are magnified in Fig. 9c. Initially, ΔR_n remains almost constant until a strain of 0.35% is reached - corresponding to a stress of 70.16 MPa - where there is a step increase to 1.22% in ΔR_n. A second step occurs at 0.46% strain, with ΔR_n rising from 2.09% to 4.11%, corresponding to 89.12 MPa. From this point on, ΔR_n increases almost linearly with the strains until the huge oscillations mentioned earlier occur.

Specimen BP-20-2 exhibits a similar behaviour to the previous specimen. The measured normalised electrical resistance increases with the stress until large electrical oscillations are recorded. The oscillation occurs at a strain of 1.5%, as depicted in Fig. 10a, corresponding to a stress of 271.78 MPa. For higher strains and during unloading, the ΔR_n-strain curve indicates the presence of damage in the specimen, as confirmed by the value of the normalised resistance after unloading. In the loading phase, the normalised resistance variation is almost constant at the beginning of the test, as shown in Fig. 10. Then, the normalised resistance increases of 1.27% with a step increment when the measured strain reaches 0.25%, corresponding to a stress of 53.10 MPa. A second step increment of 0.83% occurs at 0.34% strain (70.32 MPa), as highlighted in Fig. 10c. Although the ΔR_n increments differ between specimens, both show step increases below 100 MPa, while the specimen is still in the linear-elastic regime.

Moving on to specimens manufactured with 45 gsm BP, the overall behaviour is similar to that of the previous ones. For instance, it can be observed that the normalised electrical resistance variation increases with the strain for both BP-45-1 and BP-45-2 specimens, until significant oscillations occur. Specimen BP-45-1 shows a final normalised resistance variation of 325.09% in Fig. 11a, while Fig. 12a depicts $\Delta R_n = 48.85\%$ for specimen BP-45-2. However, the electromechanical curves depicted in Fig. 11b and 12b show differences compared to the curves obtained from specimens BP 20–1 and BP 20–2. In particular, the specimens manufactured with BP sheets of 45 gms do not exhibit the two step-increments visible on the BP- 20–1 and BP-20-2 specimens. Instead, specimens BP 45–1 and BP-45-2 reveal a smoother behaviour.

Specimen BP-45-1's normalised resistance variation features small oscillations at the beginning of the test, up to a strain of approximately 0.1%, as represented in Fig. 11b. Then, the ΔR_n exhibits a linear relationship with the strain until a strain value of almost 0.3% is reached. For higher strains, the ΔR_n increases with the strain by changing slope. A linear fitting was performed to characterise the observed electromechanical response, focusing on the linear behaviour described between the $0.1\% - 0.3\%$ strain region. The linear fitting aims to evaluate the starting and ending points of the linear behaviour in terms of strain and stress values. By doing so, it may be possible to draw some conclusions on the mechanical behaviour of the specimen based on the measured electrical resistance. The fitting was performed on the ΔR_n data in the 0.15%–0.25% strain region, resulting in the behaviour described by the equation shown in Fig. 11c, which is characterised by an R^2 value of 97.94%. The extreme strain values for which the observed behaviour

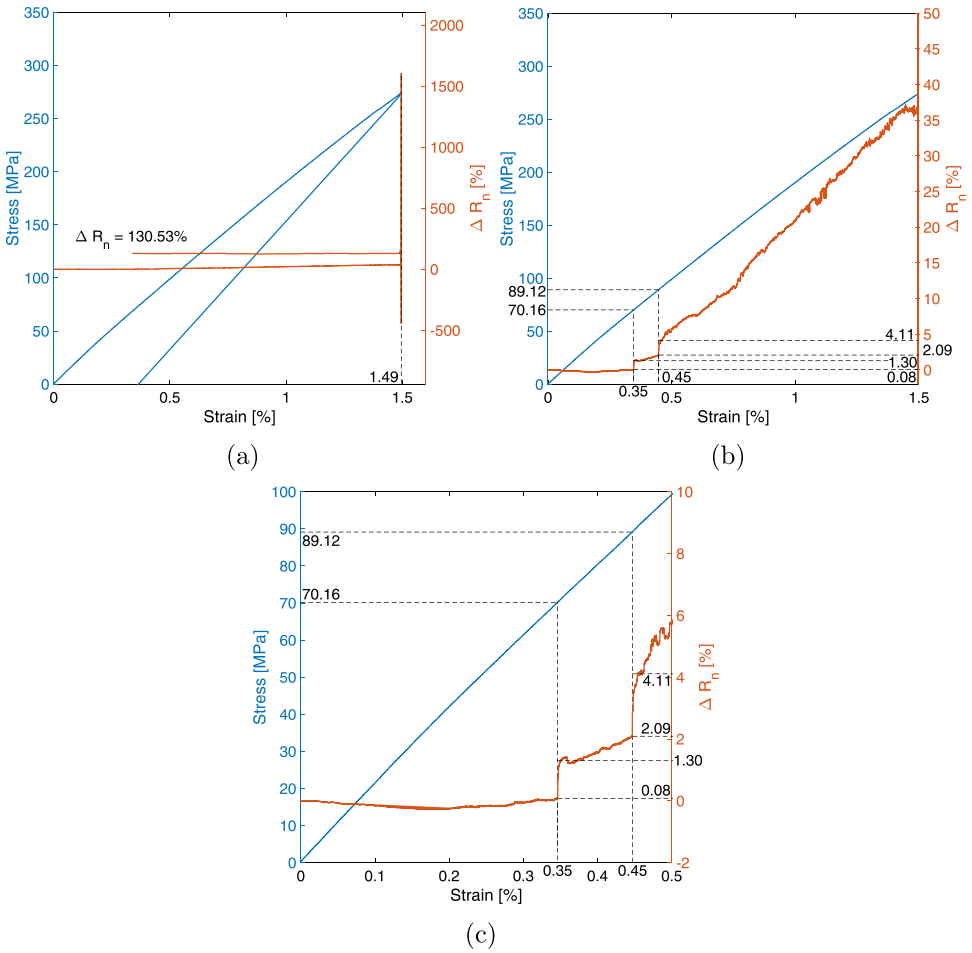

Fig. 9. BP-20-1 specimen's electromechanical curves acquired during tensile test: (a) loading and unloading phase, (b) loading phase, and (c) focus on the 0–0.5% strains region.

can be considered linear are defined as the strain value for which there is a 5% difference between the measured normalised resistance variation and the ΔR_n obtained from the linear fitting. Thus, the linear $\Delta R_n - \epsilon$ behaviour starts at 0.13% strain and ends at a strain of 0.29%, corresponding to ΔR_n values of 1.37% and 7.81% and stress levels of 32.60 MPa and 65.21 MPa.

Moving on to specimen BP-45-2, the behaviour shown in Fig. 12 is similar to that represented in Fig. 11 for specimen BP-45-1. The difference between the two samples lies in the behaviour of the normalised resistance at the beginning of the test. Specimen BP-45-2 is characterised by an increase in ΔR_n at the beginning of the test, as opposed to the small oscillations around a constant value observed for specimen BP-45-1. However, even in this case, a linear behaviour can be observed between strains of 0.1% and 0.2%. The linear fitting was performed considering the data belonging to the 0.09%–0.18% strain interval. The region for which the equation reported in Fig. 12c is valid was determined using the same criterion used for BP-45-1. As can be seen in Fig. 12c, the region in which the ΔR_n behaviour can be considered linear spans from strains of 0.06% to 0.24%, corresponding to stress levels of 15.94 MPa and 54.03 MPa and ΔR_n values of 1.19% and 6.11%. By comparing the two specimens manufactured with the 45 gsm buckypaper sheet with those manufactured with the previous two, it is evident that the linear $\Delta R_n - \epsilon$ in the 45 gsm specimens starts at a significantly lower strain value (0.06%–0.11%ϵ) than the strain at which the first step increment occurs on the BP-20-1 (0.28%ϵ) and BP-20-2 specimens (0.23% strain). This can be attributed to the improved sensing capabilities of buckypapers with higher surface densities, as indicated by the lower electrical resistance value shown in Table 4.

Figs. 13a and 14a show the electromechanical curves obtained during the tensile test for specimens BP-60-1 and BP-60-2. The overall behaviour is similar to that of previous specimens: ΔR_n increases during the test until a 1.5% strain, where huge oscillations occur for both specimens. The normalised electrical resistance of the BP-60-1 specimen is 171.34% when unloading, while that of BP-60-2 is 4995.89% after the test. Examining the electrical behaviour of these specimens more closely, Figs. 13b and 14b show a decrease in the ΔR_n value at the beginning of the test. The decrease in normalised resistance may be due to the Poisson effect: the elongation of the specimen causes a reduction in the cross-sectional area, allowing the formation of new conductive channels due to the decreased transversal distance between the nanotubes. This behaviour differs from what was observed with the Type-1 specimens with 20 gsm and 45 gsm, but it can be explained by the higher MWCNT content of these specimens compared to the others. The increased MWCNT content enables the formation of new transversal electrical paths that could not be formed with lower MWCNT content because the distance between the nanotubes was greater than what is required for the tunnelling effect to occur. However, the decrease in normalised resistance ends at strains of 0.14% and 0.18% for specimens BP-60-1 and BP-60-2, respectively. Beyond these values, the applied strains are sufficient to increase the distance between nanotubes, potentially breaking electrical channels and causing an increase in electrical resistance.

Focusing on specimen BP-60-1, in Fig. 13 it is evident that the ΔR_n value decreases linearly with the strain. Thus, a linear fitting was performed on the values in the 0%–0.1% strain range, resulting in the linear relationship reported in Fig. 13c with an R^2 value of 98.62%.

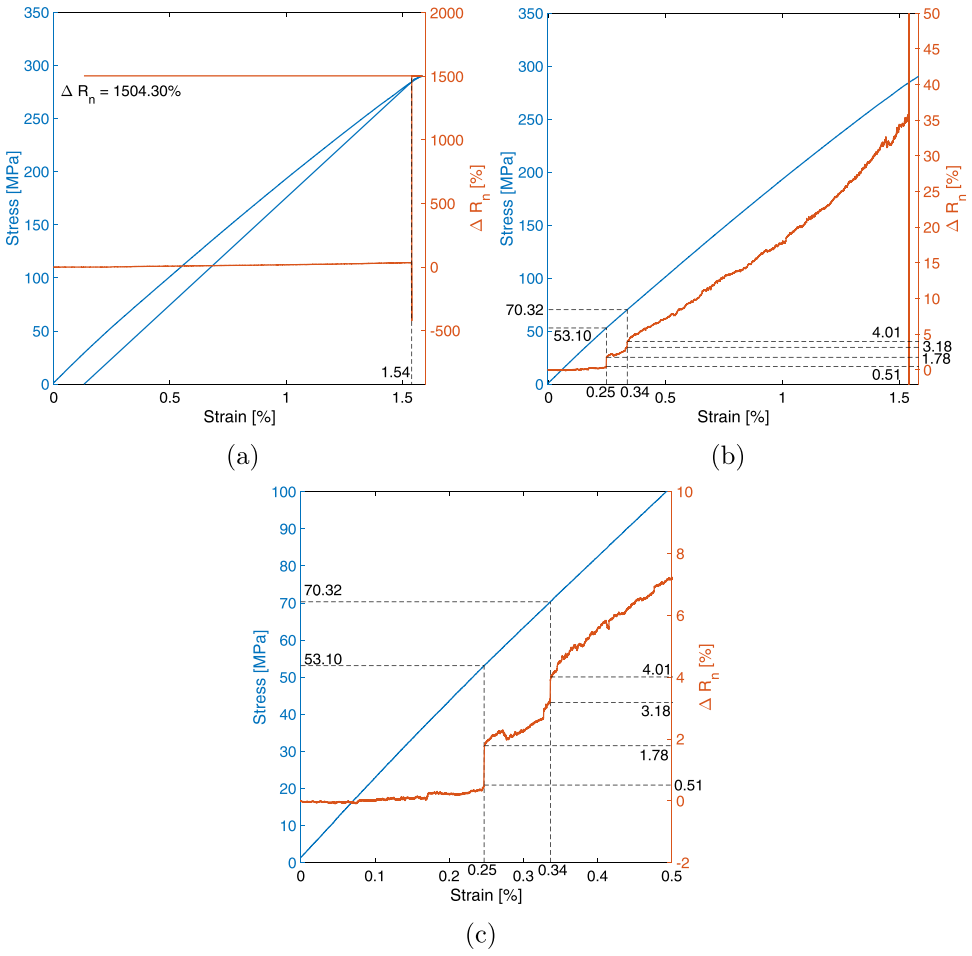

Fig. 10. BP-20-2 specimen's electromechanical curves acquired during tensile test: (a) loading and unloading phase, (b) loading phase, and (c) focus on the 0–0.5% strains region.

Adopting the same criteria as those for the Type-1 specimens with 45 gsm BP, the limit strain was found to be 0.14%, corresponding to 31.80 MPa of stress and a ΔR_n of −1.05%. Beyond this value, the normalised electrical resistance variation starts to increase with the applied load. However, another interesting observation can be found at a strain of 0.24% (51.60 MPa), the normalised electrical resistance variation undergoes a relatively small step increment, shifting from −0.53% to −0.14% for a total ΔR_n of 0.39%.

Similarly, Fig. 14 shows that the electrical resistance decreases linearly at the beginning of the test, following a slight increase for specimen BP-60-2. For this specimen, the linear fitting was applied to the data in the 0.03%–0.13% strain range. The equation reported in Fig. 14c describes the $\Delta R_n - \epsilon$ relationship, although the R^2 value of 87.89% is lower for this specimen compared to BP-60-1. The end of the linear region was found to occur at a strain of 0.18% by using the same criterion as before. Beyond the linear region, the electrical resistance increases again without showing a step increment. However, its ΔR_n increases rapidly and with a step-shaped curve between strain values of 0.23% and 0.24%, passing from −0.23% to 0.24%, for a total increment of 0.47%. The step-like normalised electrical resistance variation is almost the same value between specimens BP-60-1 and BP-60-2, which is also true for the strain values at which the step-like increment occurs. As a result, the stress state corresponding to these increments is also similar between the two samples, with the stress for specimen BP-60-1 being 51.60 MPa, and for specimen BP-60-2, the mean stress value, taken between 48.46 MPa and 51.74 MPa, is 50.10 MPa.

The reduced variation of ΔR_n in the 60 gsm buckypaper specimens compared with 20 and 45 gsm BP is attributed to the higher CNT content, which generates a denser conductive network and lower baseline resistance. As a result, resistance changes due to micro-damage or low strain are partially masked by the redundancy of conductive paths. Nevertheless, the increased conductivity also enables the observation of phenomena such as resistance reduction induced by the Poisson effect, highlighting the complex interplay between CNT content, conductivity, and sensing sensitivity.

Analysing the tensile test results from a monitoring perspective, an interesting trend emerges. Specimens manufactured with 20 gsm buckypapers exhibit two-step increments in ΔR_n for stress values below 100 MPa at strains of around 0.35% and 0.45% for specimen BP-20-1 and at 0.25% and 0.35% for BP-20-2. Step increments in normalised resistance are usually associated with damage, but the specimens' mechanical behaviour remains linear. Similarly, when the buckypaper with 45 gsm is used, the linear behaviour observed previously starts at strains of around 0.13% and 0.06% and ends at 0.29% and 0.24%, for specimen BP-45-1 and BP-45-2, respectively.

Finally, specimens made with 60 gsm buckypapers exhibited (i) linear behaviour up to strains of 0.13% and 0.14%, for specimen BP-60-1 and BP-60-2, respectively, and (ii) a step-like normalised resistance increment between the strains of 0.23% and 0.24%. Interestingly, these values are consistent with the results from the previous specimens, with the only exception being specimen BP-20-1. Specifically, the strain range of 0.23–0.25% is significant since it is in this range that step increments are observed for BP-20-1 and both BP-60 specimens. Similarly, the strain associated with the end of the linear behaviour of specimen BP-45-2 falls within this range, while the linear region for specimen BP-45-1 ends shortly after. The stress value in this strain range is around 50 MPa, which is relatively low, and as such, the overall mechanical

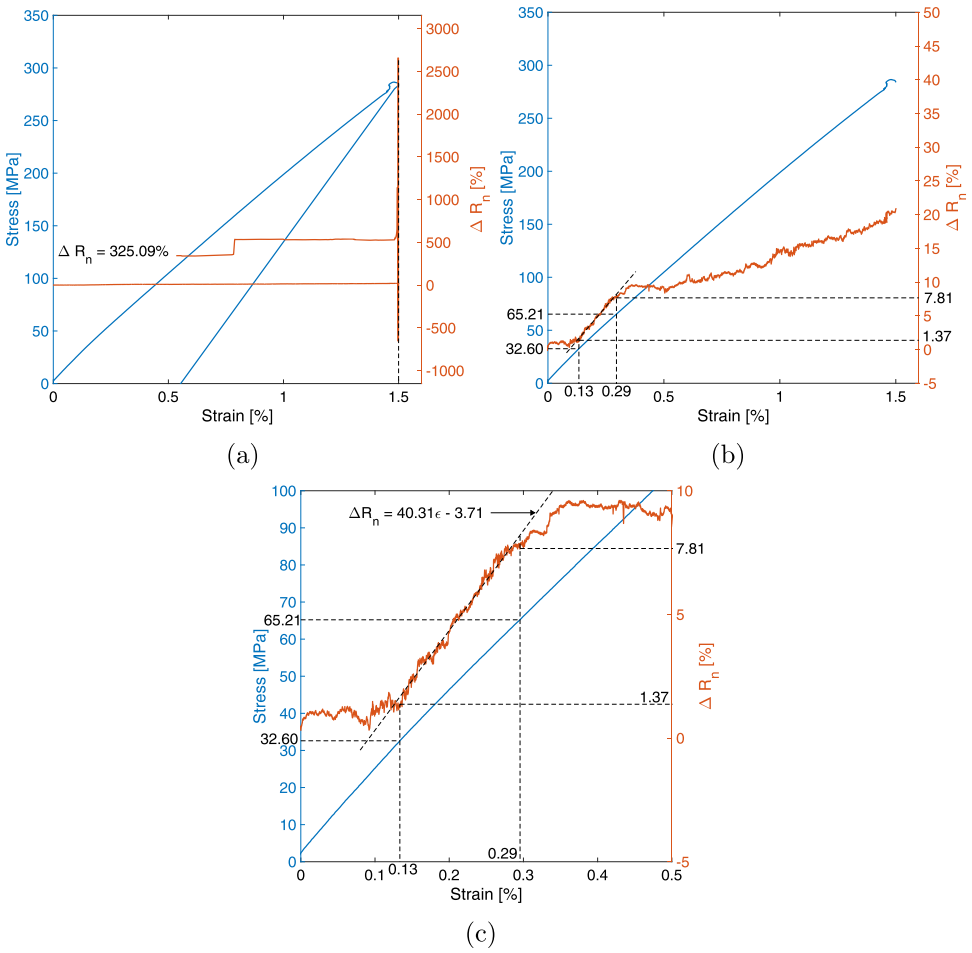

Fig. 11. BP-45-1 specimen's electromechanical curves acquired during tensile test: (a) loading and unloading phase, (b) loading phase, and (c) focus on the 0–0.5% strains region.

behaviour of the specimen is still linear. However, similar low stress values have been associated with the initiation of micro-damage in the material [50–53]. Similarly, the 50–70 MPa stress range has been associated with interfacial debonding between BP and FRP matrices [54, 55]. This suggests that the micro-damage detected at this stage can be attributed to early interfacial degradation, which was regarded as minor damage in this study in the context of the tensile response of GFRP. This aligns well with the step resistance increments shown by the specimens manufactured with 20 gsm and 60 gsm buckypapers, as they are usually associated with damage formation. Regarding specimens BP-45-1 and -2, their apparently different behaviour can be explained by variations in electrical conductivity, such as the MWCNT content. They are more conductive than BP-20 specimens but less conductive than BP-60 specimens. Therefore, the linear behaviour shown by the BP-45 specimens may be due to the improved sensing ability compared to the specimens manufactured with 20 gsm buckypapers. Therefore, they may be able to detect the entire damage formation process, as reflected in the linear relationship between normalised resistance variation and strain, which begins before and extends beyond the critical strain range of interest. One might expect the specimens manufactured with 60 gsm buckypapers to behave similarly. However, as previously discussed, the higher MWCNT content in these specimens causes the normalised resistance variation to be dominated by the Poisson's effect at the beginning of the test.

Overall, the tensile tests proved that the addition of buckypapers does not affect the mechanical strength of the GFRP composites. Furthermore, the three types of buckypaper used - 20, 45, and 60 gsm - can detect the formation of micro-damage in the material. Notably, the stress value associated with the formation of micro-damage aligns with the fatigue strength of heterogeneous materials [50–53], including the GFRP specimens used in this study.

4.2. LVI tests

Low-Velocity Impact (LVI) tests at 30.41 J were conducted on Type-2 specimens using a drop tower and an impactor, according to the ASTM D7136 standard [48]. Specimens BP-20-A, BP-45-A and BP-60-A were impacted on the rear side, which is the face furthest the buckypaper in Fig. 1, while specimens BP-20-B, BP-45-B and BP-60-B were impacted on the front side, i.e., the face closest to the buckypapers in Fig. 1 and Table 2. This was done because, depending on the impact location, the buckypapers could experience either tensile or compressive strains, as illustrated in Fig. 4. Before discussing the results of this test, it should be noted that an error in the data acquisition system prevented the recording of data during the test for specimen BP-20-A. However, the electrical resistance before and after the test is known and reported in Table 5 for all three channels. Table 6 shows the normalised resistance variation for the three channels during the LVI test. The tables report the ΔR_n, R_0, and R_f values for all specimens.

Starting with the analysis of the test results, the first step is to observe if the addition of buckypapers has any influence on the energy absorbed by the specimens. Fig. 15 shows the force–displacement curves for specimens BP-20-B in blue, BP-45-A in red, BP-45-B in green, BP-60-A in yellow and BP-60-B in purple. The curves presented in Fig. 15 allow the estimation of the energy absorbed by the specimens, which is reported in Table 7. By examining the table, it is evident that the

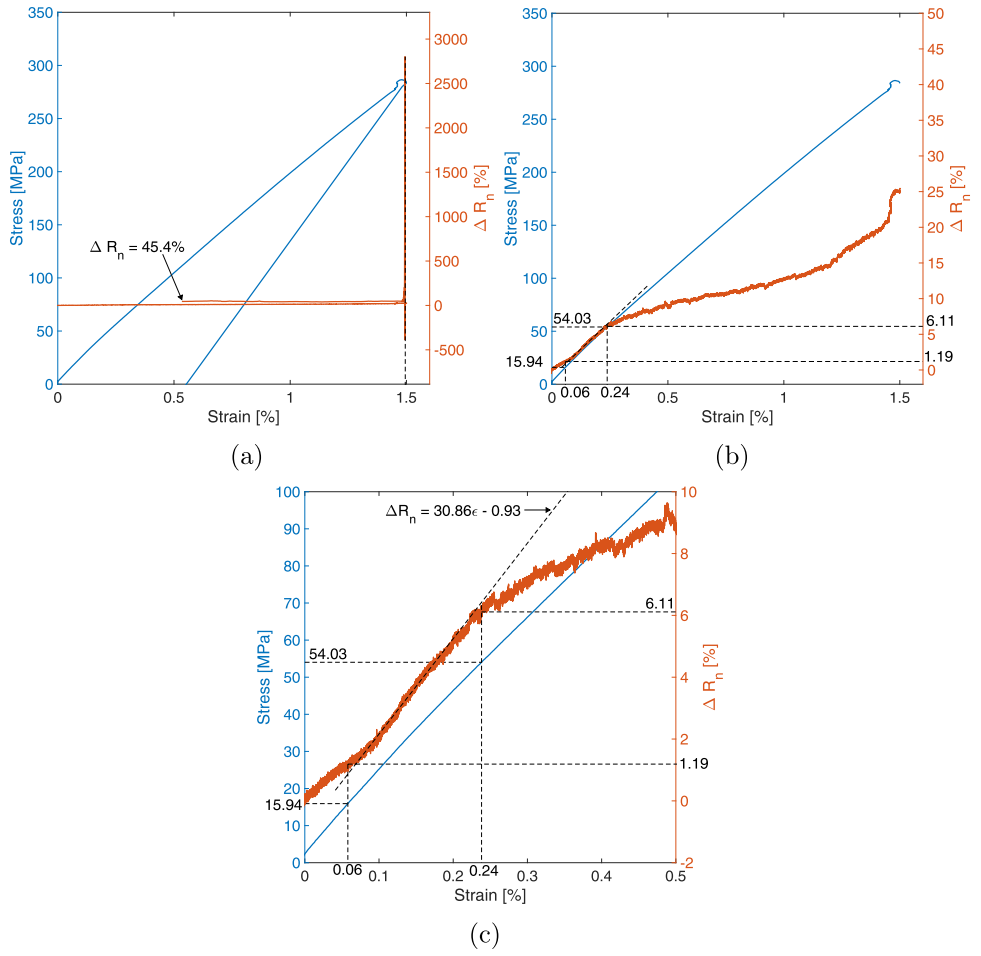

Fig. 12. BP-45-2 specimen's electromechanical curves acquired during tensile test: (a) loading and unloading phase, (b) loading phase, and (c) focus on the 0–0.5% strains region.

Table 5
Electrical resistance at the beginning, R_0, and the end, R_f, of the LVI test.

[Ω]	BP-20-A		BP-20-B		BP-45-A		BP-45-B		BP-60-A		BP-60-B	
	R_0	R_f	R_0	R_f	R_0	R_f	R_0	R_f	R_0	R_f	R_0	R_f
Channel 1	5.09	5.31	5.07	5.10	2.27	2.35	2.11	2.14	1.63	1.67	1.59	1.65
Channel 2	1.55	1.59	1.50	1.49	0.60	0.62	0.63	0.63	0.45	0.46	0.45	0.46
Channel 3	1.54	1.59	1.56	1.58	0.61	0.63	0.62	0.63	0.44	0.45	0.45	0.46

Table 6
Normalised electrical resistance variation ΔR_n at the end of the LVI test.

Specimen	Channel 1	Channel 2	Channel 3
BP-20-A	4.32	2.58	3.25
BP-20-B	0.49	−0.47	1.48
BP-45-A	3.52	3.33	3.28
BP-45-B	1.42	−0.33	2.27
BP-60-A	2.45	2.22	2.27
BP-60-B	3.77	1.97	0.55

Table 7
Energy absorbed by the specimens during the impact tests.

Specimen	Impact energy [J]	Energy loss [%]
BP-20-A	–	–
BP-20-B	29.01	4.60
BP-45-A	28.65	5.79
BP-45-B	28.65	5.79
BP-60-A	29.12	4.25
BP-60-B	29.28	3.72

energy absorbed by the specimens is similar for all of them, indicating that the buckypaper (i) proximity to the impacted face and (ii) surface density do not significantly affect the energy absorption. The tensile tests indicated no significant reduction in mechanical properties due to the incorporation of buckypapers. In the impact tests (Fig. 15 and Table 7), the absorbed energy was not systematically affected by either the buckypaper areal weight or its placement relative to the impact face. Taken together, these results suggest that the addition of buckypapers with high CNT content does not negatively affect the mechanical performance of the laminates.

Moving on to the analysis of the electromechanical behaviour for impact monitoring, the following figures report the impact force in blue on the left y-axis and the normalised resistance variation for the three channels of Type-2 specimens on the right y-axis. Channel 1 is depicted in orange, Channel 2 in red and Channel 3 in black. The horizontal axis represents the test time in seconds, allowing for better visualisation of the impact dynamics. In general, the behaviour of the specimens during

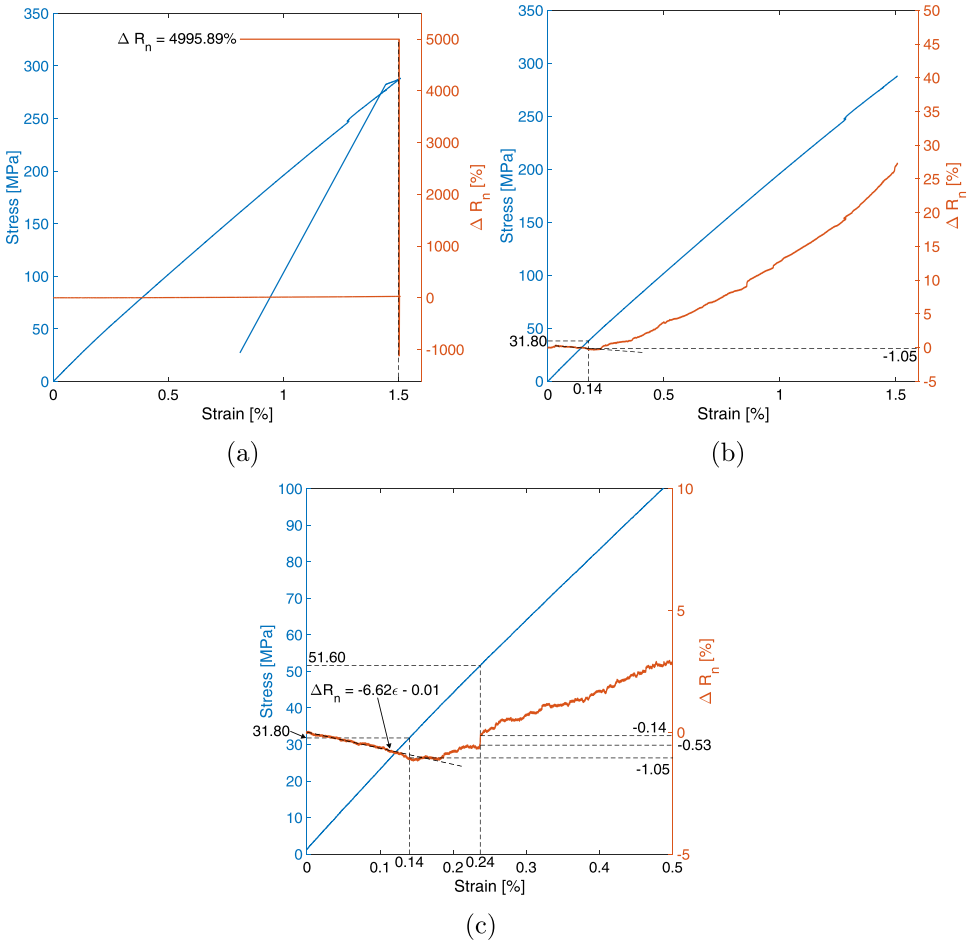

Fig. 13. BP-60-1 specimen's electromechanical curves acquired during tensile test: (a) loading and unloading phase, (b) loading phase, and (c) focus on the 0–0.5% strains region.

LVI tests can be divided into four regions, and this classification is used for the analysis of all the specimens:

- Zone 1. This is the pre-impact region. There is no load, and the electrical channels oscillate around 0.
- Zone 2. In this region, the impact event is monitored. Load and channels signals rise rapidly due to the impact. Sudden spikes in the impactor load history are strongly linked to matrix cracking and delamination, as highlighted in Figs. 16 to 20 with green and yellow boxes, respectively. The distinction between the two damage mechanisms can be made since sudden variations in the load signal are associated with matrix cracking, while less abrupt changes are linked to delamination [56–60]. Contact variations and the tunnelling distances among adjacent CNT after the onset of damage and increase in strain cause variations in electrical resistance. However, directly associating the data evolution with specific types of damage can be quite challenging because the buckypaper nanocomposite material consists of only a single layer of CNT. Therefore, the self-sensing property is expected to be affected by the relative position of the damage within the thickness of the buckypaper.
- Zone 3. After the impact, free oscillations of the specimen are observed, with the impactor bouncing back after the impact. The load signal drops to zero. Oscillations in the electrical CNT signals mirror the free vibrations of the plates. Impact force curve oscillations represent the rebounds of the impactor on an aluminium plate, which is used to avoid rebounds on the specimens, as mentioned in Section 3.3.
- Zone 4. This region is characterised by a permanent shift in normalised electrical resistance, which is associated with damage. The permanent shift is registered once the specimen oscillations have completely dampened.

Starting with specimen BP-20-B, Fig. 16 shows its electromechanical curves acquired during the test. The four regions described can be clearly distinguished, but it is hard to directly associate electrical resistance variations with damage type in Zone 2. The only electrical signal that can be correlated with the force signal is Channel 3, which shows two electrical resistance steps corresponding to the first two step increments in the impact load, as visible in the green box of Fig. 16. In addition, there seems to be a delay between the Force curve and the Channels 1 and 3 curves, with variations in Channel 3 that seem to mimic the load signal. This delay may be due to the placement of the buckypaper, which limits the sensing abilities to its location. Since specimen BP-20-B was impacted on the front face, i.e., the free surface close to the buckypaper's location, the buckypaper sheet is expected to be mainly subjected to compressive strains, which would cause the electrical resistance to decrease. However, only Channel 2 shows the expected behaviour. Specifically, it experiences a resistance step increment at the moment of the impact - i.e., corresponding to the first load step increment - and a step decrease when the force signal experiences the second step increment. This variation in the Channel 2 signal can be attributed to matrix crack phenomena as suggested in the literature [56–60]. In contrast, Channels 1 and 3 experience an increase in the measured electrical resistance. This could be due to the high stiffness of the specimens, which induces tensile membranous effects

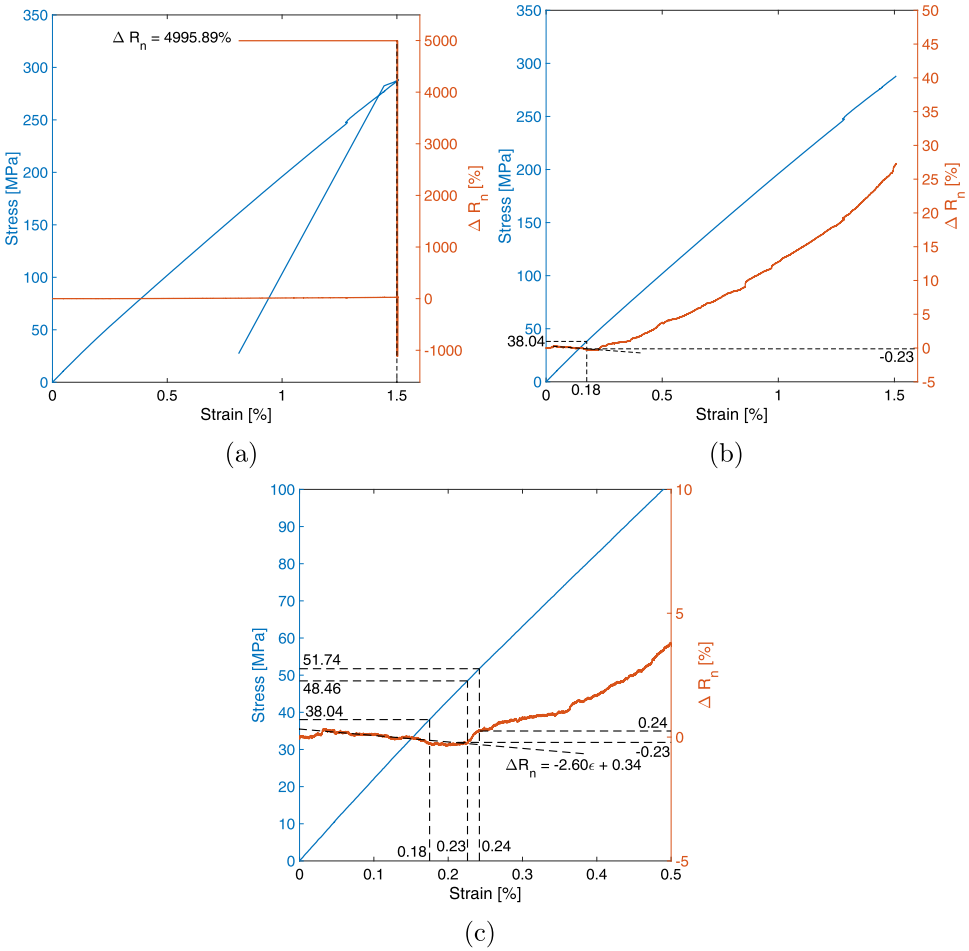

Fig. 14. BP-60-2 specimen's electromechanical curves acquired during tensile test: (a) loading and unloading phase, (b) loading phase, and (c) focus on the 0–0.5% strains region.

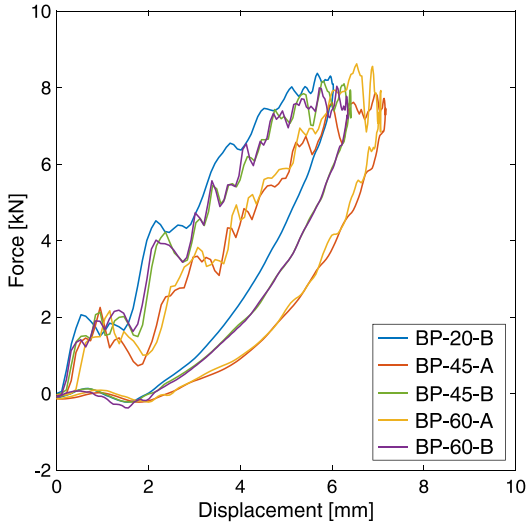

Fig. 15. Force–displacement curves of the impact tests of specimens BP-20-B, BP-45-A, BP-45-B, BP-60-A and BP-60-B. Specimen BP-20-A is missing due to an error in the data acquisition system.

that override the bending effects. In addition, the observed difference between Channel 2 and Channel 3 (around 2%) is attributed to the slightly off-centre position of the impact, which was shifted towards the diagonal connecting the Channel 3 electrodes (as will be shown in Fig. 27b in Section 4.3). Consequently, Channel 3 exhibited resistance increases associated with damage and tensile strain, while Channel 2 mainly recorded compressive strains due to its location relative to the impact. This behaviour illustrates the capability of buckypaper sensors to distinguish local strain and damage effects, which is particularly relevant for SHM applications where impact events rarely occur at perfectly symmetric positions. Regarding Zone 3, Fig. 16 shows a variation in the normalised electrical resistance towards the final value shown in Zone 4. Therefore, the oscillations of the plate are not reflected in oscillations in the electrical signals but rather in a relatively smooth variation of them towards the permanent ΔR_n shift. Since all the channels exhibit a permanent shift in normalised electrical resistance, impact-induced damage can be successfully detected. Specifically, the ΔR_n variation at the end of the test is 0.49% for Channel 1, −0.47% for Channel 2 and 1.48% for Channel 3, as shown in Table 6. Table 5 presents the values of electrical resistance before and after the LVI test.

Fig. 17 shows the electromechanical curve acquired during the LVI test performed on specimen BP-45-A. This specimen was impacted on the rear surface, so the buckypaper experiences tensile strains, and the electrical resistance should increase during the impact. The signals acquired during the test confirm these expectations. As seen in both Fig. 17 and Table 6, there is a positive final value of ΔR_n at the end of the test, indicating an increase in electrical resistance. Focusing on Zone 2, it is evident that Channels 1 and 2 present peaks in the signal, occurring in close proximity to drops in the force signal. This suggests that they are sensitive to matrix crack phenomena. Similarly, when the load signal reaches its peak and shows some oscillations, which

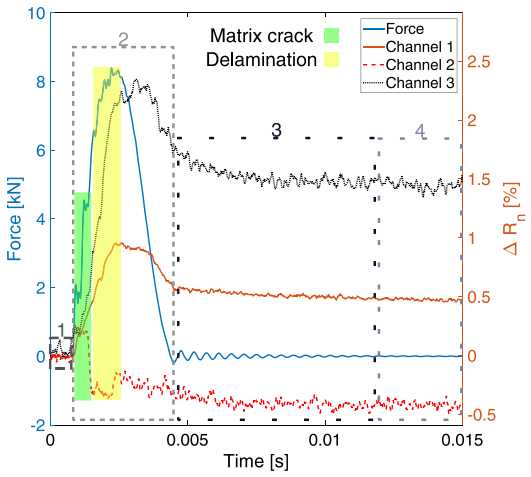

Fig. 16. Electromechanical curves of the LVI impact performed on specimen BP-20-B.

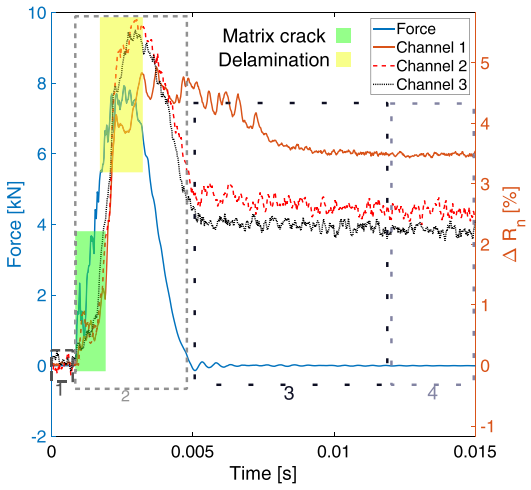

Fig. 17. Electromechanical curves of the LVI impact performed on specimen BP-45-A.

is usually associated with delamination, Channels 1 and 2 exhibit ΔR_n variations, likely related to the delamination. Channel 3 shows the same features as the other two channels but with smaller ΔR_n variations. As with the previous specimen, the oscillations of the plate in Zone 3 are reflected in asymptotic ΔR_n variations towards the permanent shift observed in Zone 4. Only Channel 1 presents significant oscillations at the beginning of Zone 3, which are not mirrored in the load signal. Therefore, they are probably associated with the initial vibrations of the plate.

Moving on to specimen BP-45-B, e.g., which was manufactured with 45 gsm buckypaper and impacted on the front side, Fig. 18 shows the electromechanical data acquired during the test. Similarly to specimen BP-20-B, which was impacted on the front side, the buckypaper is placed where compressive strains are expected, meaning that a ΔR_n decrease should be observed. However, as with specimen BP-20-B, only Channel 2 shows the expected reduction in electrical resistance, while an increase in ΔR_n can be observed in Fig. 18 for Channels 1 and 3. As previously stated, this behaviour could be explained by the presence of tensile membranous effects generated by the stiffness of the specimen. Channels 1 and 2 show electrical resistance variations indicative of matrix cracking, with Channel 1 exhibiting a relatively small drop and Channel 2 displaying a parabolic rise and fall. All channels appear to reflect the oscillations of the load signal, with

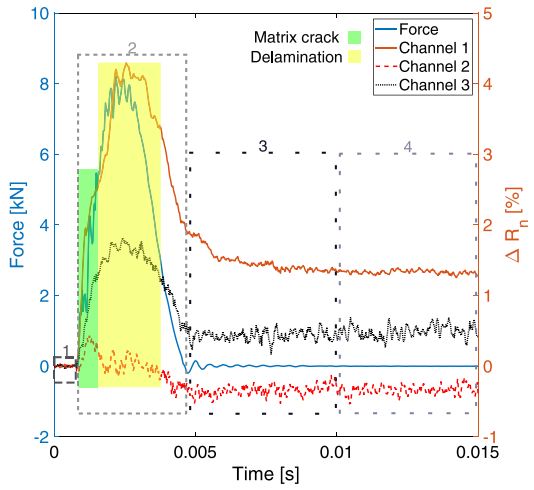

Fig. 18. Electromechanical curves of the LVI impact performed on specimen BP-45-B.

smoother variations likely associated with delamination. Similarly to the previous specimens, in Zone 3, there is an asymptotic variation of ΔR_n towards the final shift observed in Zone 4, and no channel can be directly related to the specimen's oscillations.

Fig. 19 shows the signals acquired during the impact test on the rear side of specimen BP-60-A, i.e., on the surface far from the buckypapers. Therefore, as with specimen BP-45-A, an increase in ΔR_n is expected in all the channels since the buckypaper sheet is placed on the extrados of the deformed specimen, as shown in Fig. 4. Accordingly, all three electrical channels exhibit the expected behaviour. Interestingly, Channel 3 shows a decrease in electrical resistance in the region associated with matrix crack phenomena, corresponding with abrupt changes in the impact load. However, after that, the ΔR_n value of Channel 3 rises, following the expected behaviour. Channels 1 and 2 also show sensitivity to matrix cracking, with Channel 1 exhibiting a peak aligned with oscillations in the load signal, while Channel 2 displays a drop in electrical resistance. Small spikes can be observed in all the channels when delamination occurs.

It is interesting to note that Channel 1's behaviour differs from that of the other two channels since its signal does not mimic the load signal. The ΔR_n in Channel 1 continues to increase almost until it reaches its final value, without showing a clear peak related to the impact.

As in the previous cases, Zone 3 is characterised by a decrease in ΔR_n, which then reaches the permanent shift observed in Zone 4. Once again, no channel can be directly related to the specimen's oscillations.

Specimen BP-60-B was impacted on the front face, so a decrease in electrical resistance is expected to happen during the test. However, like the other specimens impacted on the rear face, this behaviour is not observed, as can be seen in Fig. 20. Channel 1 exhibits slope changes in correspondence with the oscillations in the load signals associated with the matrix crack. Channels 1 and 2 appear to detect delamination, as Channel 1 shows a decreasing trend in normalised electrical resistance with superimposed small oscillations corresponding to fluctuations in the load signal, while Channel 2 closely mirrors the force signal's oscillatory behaviour.

Channels 2 and 3 have very similar ΔR_n variations across all the four identified regions, with Channel 2 showing a slightly higher increase in electrical resistance compared to Channel 3. Their electrical resistance immediately reaches the final values shown in Zone 4, i.e., after specimen oscillations, without the asymptotic variation observed in the previous specimens. Regarding Channel 1, after the typical peak in electrical resistance caused by the impact event in Zone 2, Zone 3 exhibits the asymptotic ΔR_n decrease, as observed in the other

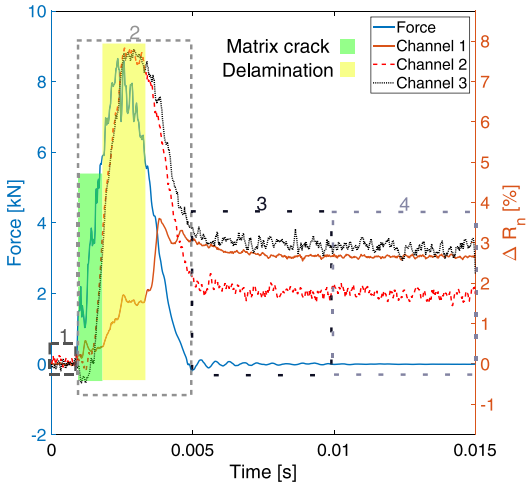

Fig. 19. Electromechanical curves of the LVI impact performed on specimen BP-60-A.

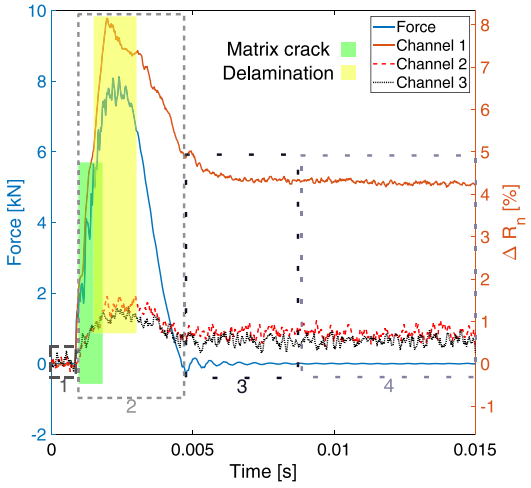

Fig. 20. Electromechanical curves of the LVI impact performed on specimen BP-60-B.

specimens. Zone 4 is characterised by the permanent ΔR_n shift for all the electrical channels.

To conclude the analysis of the Low-Velocity Impact test results, some considerations can be made:

- Regardless of the buckypaper's location at the moment of impact, whether extrados or intrados, it is possible to monitor impact events. Not only can the impact dynamics be observed through the peaks shown by the electrical channels in Zone 2, but the presence of the damage can also be detected by the permanent shift in electrical resistance, as shown in Tables 5 and 6.
- Specimens impacted on the rear side - i.e., with the buckypaper placed on the intrados of the expected deformation - consistently show lower ΔR_n variations compared to the specimens impacted on the front side, as reported in Table 6. This finding is reasonable as buckypapers further from the impact location will be less affected by the damage, provided the impact event happens under the same conditions, as in the tests presented in this study.
- Buckypaper-based monitoring can detect damage mechanisms such as matrix cracks and delaminations. Interestingly, the associated variations in electrical resistance are more pronounced when the buckypaper is positioned farther from the impacted surface. This may be due to the localised nature of buckypaper sensing, where increased ΔR_n variations result from the tensile strains experienced by the buckypaper when it is located away from the impact zone. However, as observed in Section 4.1, buckypapers allow the highest conductivity to be used, i.e., the best sensitivity, without the risk of CNT agglomeration that can occur when dispersing CNT inside the matrix, which is detrimental for the mechanical properties.

Table 8
Estimated buckling loads and displacements.

Specimen	Buckling load [kN]	Buckling displacement [mm]
BP-20-A	57.66	2.09
BP-20-B	52.34	1.66
BP-45-A	56.32	2.06
BP-45-B	53.60	2.14
BP-60-A	65.59	2.16
BP-60-B	67.38	2.11

4.3. CAI tests

Compression After Impact (CAI) tests are conducted to assess the post-impact-induced damage sensing capabilities of impacted specimens. Specifically, this test aims not only to compare the sensing abilities of damaged sensor networks featured by different electrical conductivities but also to investigate whether it is possible to detect the onset of buckling phenomena. The latter is valuable as it can be used to prevent the material from reaching this instability.

Before analysing each specimen, the critical buckling load P_{cr} was identified by performing a linear fitting of the compressive force curve's linear region, within the 1.0–1.5 mm displacement range. The buckling load was defined as the acquired compressive load value at which the error between the fitting and force reaches 5%. The displacement value associated with the buckling load is referred to as the buckling displacement. Table 8 shows the buckling loads identified in this way for all the tested specimens. Fig. 27 presents the specimens after the CAI test.

Starting with specimen BP-20-A, Fig. 21 shows the electromechanical curves acquired during the CAI test. At the beginning of the test, the electrical resistance of the channels does not change significantly, oscillating around zero. This behaviour is due to the preliminary loading phase during which the compressive load is relatively low. As the compressive load increases, the electrical channels exhibit different behaviours. Channel 2 experiences a decrease in electrical resistance up to approximately 1.20 mm. Beyond this point, Channel 2's electrical resistance starts increasing. In contrast, Channels 1 and 3 experience an increase in normalised resistance until a displacement of 2.24 mm of the test-machine crosshead, as shown in Fig. 21. A slope change in the electrical resistance of Channels 1 and 3 is observed at this displacement value, together with a drop in the force curve. This behaviour can be associated with damage occurring in the specimen. From this point on, Channel 1's normalised resistance is almost constant, while the electrical resistance of Channel 3 decreases.

The different behaviour shown by Channel 2 compared to Channels 1 and 3 can be explained by examining Fig. 27a. The impact location is not centred on the plate, but rather shifted slightly on the right. Thus, the damage primarily affects Channel 2 (defined as in Fig. 6), which shows a significant increase in electrical resistance during the test. In addition, the electrical resistance of Channel 2 may initially decrease at the beginning of the test because of the compressive force, which tries to cause CNTs in the damaged area to move closer together.

The analysis of the CAI test involves identifying the buckling load, which is evaluated as previously described at the beginning of this section. Using that procedure, a buckling load of 57.66 kN can be identified, corresponding to a displacement of 2.09 mm. Fig. 21 also

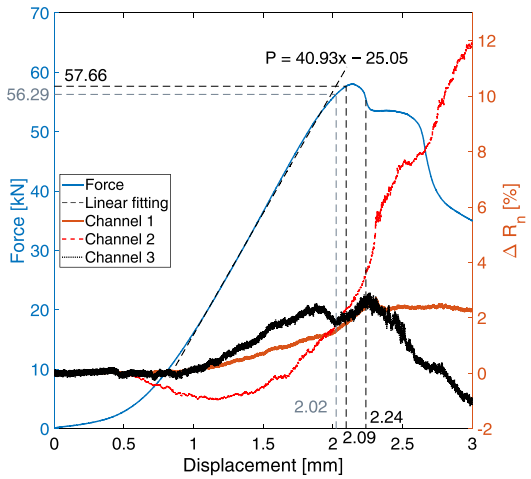

Fig. 21. BP-20-A specimen's electromechanical curves acquired during CAI test and evaluation of the critical buckling load.

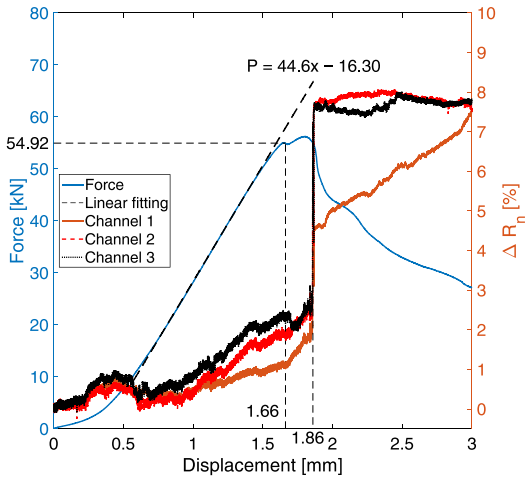

Fig. 22. BP-20-B specimen's electromechanical curves acquired during CAI test and evaluation of the critical buckling load.

shows the linear fitting and the estimated critical buckling load. In this figure, it can be observed that Channels 1 and 3 electrical resistance starts increasing when the load curve approaches its linear region. In addition, both channels exhibit a slope change at 2.02 mm, which is 0.07 mm before the displacement associated with the identified buckling load, i.e., 1.37 kN before the critical buckling load, meaning that buckling onset can be detected. Channel 3 also exhibits a drop in electrical resistance at 1.90 mm, which is before the 2.02 mm identified earlier.

Specimen BP-20-B was impacted on the front side and, as shown in Fig. 27b, the damage is centred. All the channels are expected to be affected in almost the same way due to the damage location. In contrast to the previous specimen, the buckypaper is far from the damaged region, so a different behaviour is expected compared to specimen BP-20-A. Fig. 22 shows the electromechanical curves acquired during the CAI test. It is immediately noticeable that, in contrast to specimen BP-20-A, the three electrical channels show the same behaviour, with only slight differences. At the beginning of the test, the ΔR_n value oscillates around zero for all channels. Then, as the load approaches linear behaviour, the electrical channels exhibit a parabolic increase and a decrease in normalised electrical resistance, which ends at the beginning of the linear loading phase. Fig. 22 reports the fitting describing the compressive load behaviour as a function of the crosshead displacement in the linear region. From this, the buckling load is identified as 54.92 kN, corresponding to a displacement of 1.66 mm. Then, after buckling occurs, the load continues to increase until it starts decreasing at 1.86 mm. A step increment in electrical resistance is registered at this crosshead displacement value, indicating that damage occurred. Accordingly, Fig. 27b confirms that damage took place during the test as the surface of the specimen is damaged near the three upper connections of the electrical channels. While specimen BP-20-A provided indicators of local buckling occurrence, such as a drop in resistance and slope changes, specimen BP-20-B did not exhibit any sign of buckling occurrence. This may be due to the buckypaper's location because it is close to the damage for specimens impacted on the front side, and far from the damage for those with rear side impacts. Therefore, when the buckypaper is close to the damage location, the compressive strain field may allow the re-creation of conductive channels previously affected by the damage. This could lead to an increase in electrical conductivity, masking any indicators of the ongoing buckling. However, a parabolic increase and a decrease in electrical resistance is observed around a displacement of 0.5 mm for all channels. The end of this quadratic trend aligns with the beginning of the linear force–displacement field, which can be related to the generation of a uniform compressive strain field in the specimen.

Moving on to specimen BP-45-A, Fig. 23 shows the signals recorded during the test. Channel 1 experiences a significantly larger ΔR_n variation compared to the other two channels. Therefore, Fig. 23a primarily focuses on the normalised resistance variation of Channel 1, while Fig. 23b represents Channels 2 and 3. As the impact location is positioned along the specimen's vertical axis of symmetry, a similar behaviour can be expected between the channels. Channels 2 and 3 are very close since the electrical resistance variation curves are qualitatively similar and have comparable final normalised resistance values. However, Channel 1 experiences much higher ΔR_n variations compared to the other two channels, even though the overall shape of the curve is similar. Channel 1 exhibited increased electrical resistance when the load–displacement relationship had already become linear. This behaviour change corresponds to an increase in electrical resistance for Channels 2 and 3 soon after a crosshead displacement of 0.5 mm and can be related to the achievement of a homogeneous distribution of the compressive stress field.

The load–displacement linear relationship is reported in Fig. 23a. A buckling load of 55.88 kN is determined, corresponding to a crosshead displacement of 2.06 mm. Before reaching this critical condition, a huge step increment can be observed in Channel 1, with a ΔR_n of 12.48% at 1.89 mm, as shown in Fig. 23a. However, Fig. 23b does not show any clear signs or preliminary indicators that could serve as a warning for the impending buckling. There is a small variation in the electrical resistances of Channels 2 and 3 at 1.89 mm, but the variation is too small to be used as an indicator.

Channel 1 exhibits a second step increment in normalised resistance with the maximum acquired load value and then remains almost constant, except for oscillations in the final part of the test. Channels 2 and 3 have similar oscillations, which correspond to the second knee in the force signal. Fig. 27c reveals a possible breakage in the upper section of specimen BP-45-A, where it was mounted on the test fixture. However, no visible damage appears in the central region, which is the sensed area. Therefore, the knees in the loading curve relate to damage in the upper part of the specimen, while the electrical oscillations may result from vibrations caused by that damage.

Addressing specimen BP-45-B, no indicator of buckling onset is expected based on the comparison between specimens BP-20-A and BP-20-B. The three electrical channels exhibit almost the same behaviour, and their ΔR_n variation is smooth throughout the test, as shown in Fig. 24. Channels 2 and 3 reach the maximum value of normalised resistance soon after buckling occurs, which was identified to happen

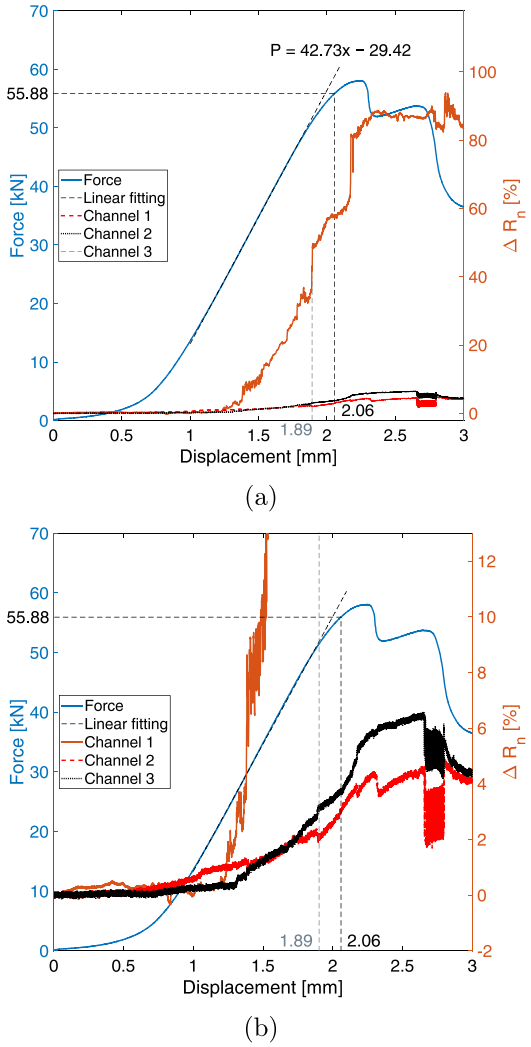

Fig. 23. BP-45-A specimen's electromechanical curves acquired during CAI test and evaluation of the critical buckling load: (a) Channel 1, and (b) magnification to better visualise Channels 2 and 3.

at 2.14 mm. In contrast, Channel 1's electrical resistance continues to increase without showing any peculiar behaviour. This could be due to damage propagating in the upper part of the specimen, as shown in Fig. 27c. The damage originated close to the fixture at the left and right borders and then spread towards the centre. It appears to be limited to Channel 1's area of influence, explaining why this channel behaves differently from Channels 2 and 3. The linear fitting used to perform buckling load identification is reported in Fig. 24.

As observed for the specimens manufactured with 20 gsm buckypaper, it is not possible to have buckling onset alarms when the buckypaper is placed close to the damage. However, for specimen BP-45-B, it is noticeable that the electrical resistance exhibits a more pronounced increasing trend when the load–displacement relationship becomes linear, around 0.7 mm in Fig. 24 since the electrical resistance varies almost linearly with the crosshead displacement for all channels.

Moving onto specimens manufactured with the highest conductivity buckypaper, specifically 60 gsm buckypapers, we shall begin with specimen BP-60-A, which was impacted on the rear side. Fig. 25a shows the entire normalised resistance variation during the CAI test. It is evident that there are two significant electrical resistance step increments when the crosshead displacement is 2.40 mm and 2.47 mm. These increments in electrical resistance are mirrored by decreases in compressive load, indicating damage formation. This is clearly visible in Fig. 27e, where

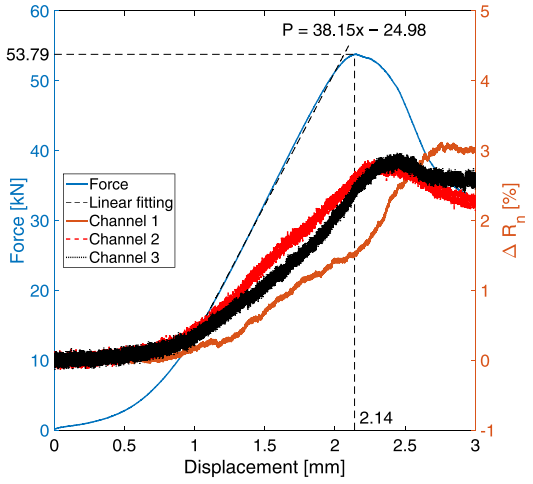

Fig. 24. BP-45-B specimen's electromechanical curves acquired during CAI test and evaluation of the critical buckling load.

two areas of damage in the central part of the specimen can be seen. One damage starts immediately under the upper electrical connections and goes from the left towards the right, stopping near Channel 3's electrical contact. The other damage, starting from the right side of the specimen, extends towards the impact damage induced by the LVI test. These are indicators of global buckling.

However, Fig. 25b focuses on the variation of electrical resistance during the test, excluding the step increments because in Fig. 25a it is not possible to appreciate ΔR_n variations before the step increments. Fig. 25 also reports the equation obtained from the linear fitting used to identify the buckling load. Analysing the signals reported in Fig. 25b is particularly interesting because they reveal different behaviours:

- Channel 1 reports a decrease in electrical resistance up to 1.50 mm. Conversely, Channels 2 and 3 show an increase in electrical resistance. The different behaviours can be explained by referring to Fig. 6b. In this figure, Channel 1 is vertical, so the distance between the electrical terminals decreases during the test due to compression. This implies that the distance between adjacent carbon nanotubes decreases, allowing (i) the creation of new contacts between CNT and (ii) the activation of new conductive paths if the distance between nanotubes falls below the tunnelling distance, i.e., 1.8 nm. These phenomena dominate the decrease in Channel 1's electrical resistance until 1.50 mm. Beyond this point, the high compressive load induces damage mechanisms, such as matrix cracking, which increase the electrical resistance. In contrast, Channels 2 and 3 are placed along the diagonals of the specimen. This implies that as the compression progresses, the distance between the electrical terminals of the channels increases due to Poisson's effect, because the specimen tries to expand horizontally in response to the vertical compression. The reason these effects are noticeable in specimen BP-60-A and not in the previous four specimens can be attributed to the different conductivity of the buckypaper used. These effects only become relevant with the buckypaper with the highest CNT surface density, i.e., the best conductivity.
- Channel 1 shows a higher ΔR_n decrease rate, i.e., slope change, at 0.66 mm of displacement, while Channels 2 and 3 start to show an increase in electrical resistance. This happens when the load–displacement curve begins its linear region, as also observed in the previous specimens.
- Channels 2 and 3 exhibit a significant slope change towards higher electrical resistances when the crosshead displacement is approximately 2.03 mm, corresponding to a compressive load of

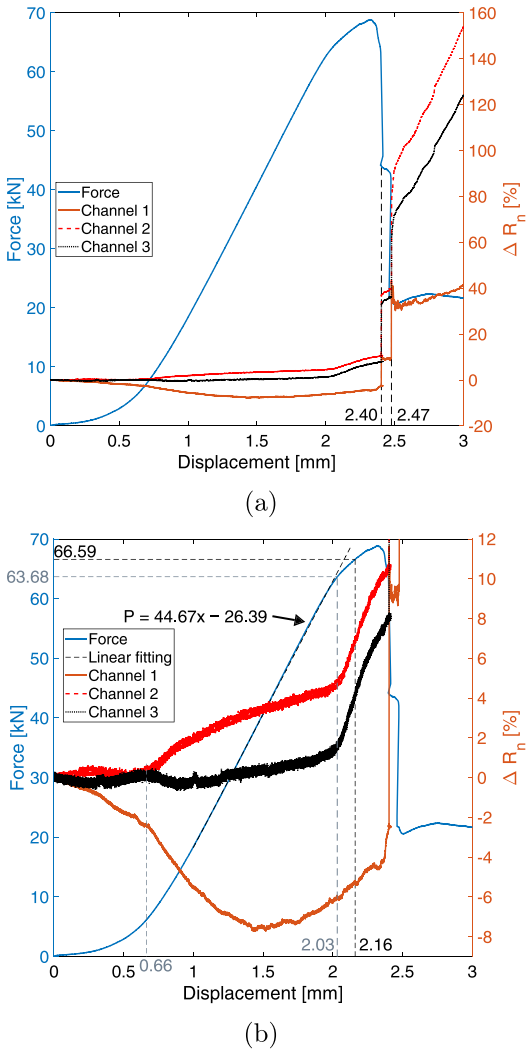

Fig. 25. BP-60-A specimen's electromechanical curves acquired during CAI test: (a) electromechanical curves and (b) evaluation of the critical buckling load with magnification to better visualise ΔR_n variations before the step increment.

63.68 kN. This can be interpreted as a sign of buckling onset since the identified buckling load of 66.59 kN occurs at 2.16 mm of displacement. However, thanks to its high conductivity, this specimen provides two indicators before buckling. The first is the aforementioned ΔR_n slope increase of Channels 2 and 3, and the second occurs at 1.50 mm when the electrical resistance of Channel 1 stops decreasing since the compressive load is high enough to induce damage.

Regarding the last specimen, BP-60-B, the electromechanical curves acquired during the tests are depicted in Figs. 26a and 26b. Fig. 26b is used to highlight the normalised resistance variations occurring before the huge step increment observed at 2.59 mm of displacement shown in Fig. 26a, similar to the test for specimen BP-60-A. In Fig. 26a, a drop in the compressive load is registered simultaneously with the step increment in electrical resistance at 2.59 mm, indicating that damage has occurred in the specimen. This is confirmed in Fig. 27f, where the damage is clearly visible. The damage extends across the entire width of the specimen, passing by the damage caused by the impact test, providing evidence of global buckling, similar to specimen BP-60-A.

Focusing on Fig. 26, different behaviour between the electrical channels can be observed. Similar to specimen BP-60-A, Channel 1 shows a decrease in electrical resistance up to almost 1.99 mm. Beyond this point, its electrical resistance increases rapidly. The explanation for this behaviour is the same as for specimen BP-60-A: initially, the compressive load facilitates the creation of new conductive pathways, but once the compressive load is high enough to induce damage, the electrical resistance increases due to damage formation. In contrast, Channels 2 and 3 seem to exhibit mirrored behaviour until buckling occurs. Both channels show a general increasing trend, with Channel 2 experiencing a decrease in ΔR_n at the beginning of the test and at 0.78 mm, and Channel 3 showing an increase in electrical resistance.

In addition, similarly to the other specimens, a change in electrical resistance can be associated with the beginning of the linear field of the load–displacement curve. This occurs at 0.78 mm of displacement, where Channel 1 shows a higher normalised resistance decrease rate, Channel 2 starts to exhibit a decrease in ΔR_n, and Channel 3 undergoes a more pronounced increase in electrical resistance.

Based on the findings evidenced from previous specimens, one would not expect signs of buckling onset, as observed in other specimens impacted on the front side. Fig. 26b partially contradicts this statement because, while it is true for Channels 2 and 3, the same cannot be said for Channel 1. The latter shows a significant ΔR_n increment at 1.99 mm of displacement corresponding to a load of 64.59 kN, which is lower than the identified buckling load of 67.38 kN, which occurs at a displacement of 2.11 mm This finding is crucial because it indicates that buckling onset can be detected regardless of buckypaper placement relative to the damage location when using 60 gsm buckypapers. This is not the case for buckypapers with lower conductivities, since buckling indicators were only observed if the buckypaper was placed far from the damage, as the compressive load masks buckling indicators by enhancing the formation of conductive paths disrupted by the damage induced during LVI tests.

It is worth delving into the behaviour of specimens BP-60-A and BP-60-B, as they demonstrated the best performance from a Structural Health Monitoring perspective. The electrical channels of both specimens exhibit similar features during the test. However, there are some differences, such as the different load and displacement values at which changes in normalised resistance behaviour are detected. For instance, Channel 1 ΔR_n starts increasing at 1.5 mm (63.68 kN) for specimen BP-60-A and at 1.99 mm (64.59 kN) for specimen BP-60-B. A possible explanation for this could be the distance of the buckypaper relative to the damage location: the buckypaper is closer to the damage in specimen BP-60-B since it was impacted on the front side. Therefore, the compressive strain field facilitates the re-creation of some of the conductive paths that were broken during the impact test, delaying the displacement value at which the electrical resistance starts increasing. This reasoning also helps explain the change in slope towards a lower decreasing rate that occurs just before 1.5 mm displacement in specimen BP-60-B. The reduced rate of decrease in electrical resistance could be due to the combined effects of the mechanisms creating new electrical paths, enhancing electrical conductivity, and the onset of damage, which increases electrical resistance.

In addition, the load and displacement values associated with the buckling condition are very similar for these two specimens, while the critical loads are almost 10 kN lower for other specimens. Similarly, Figs. 27e and f show similar damage in the central region of the specimens, while the specimens manufactured with 45 gsm and 20 gsm buckypapers show damage in the upper part of the specimen, close to the upper fixture. These differences may be attributed to an improper fixing of the first four specimens, leading to actual buckling only in the BP-60-A and BP-60-B specimens.

It is worth quantifying the influence of BP areal density on detection sensitivity. As shown in Table 5 (Type-2 specimens), the initial resistance decreases as the areal density increases, confirming that higher CNT loading leads to denser conductive networks. This trend is consistent with the tensile test results reported in Table 4 (Type-1 specimens).

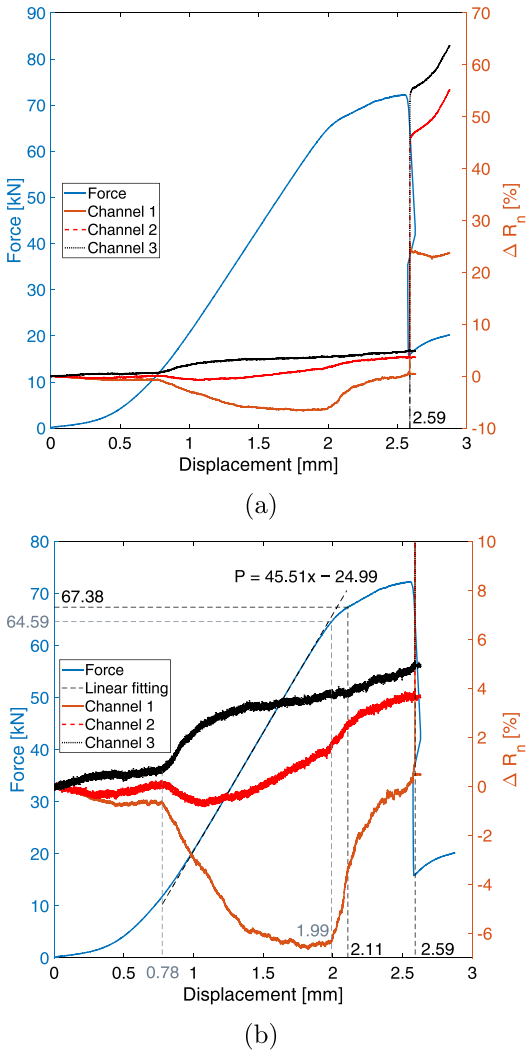

Fig. 26. BP-60-B specimen's electromechanical curves acquired during CAI test: (a) electromechanical curves and (b) evaluation of the critical buckling load with magnification to better visualise ΔR_n variations before the step increment.

A denser network enhances sensitivity to small variations in CNT–CNT distances induced by strain or damage, since a larger number of conductive pathways can be disrupted or reconfigured. This effect is directly reflected in the CAI results since specimens with lower areal density (20 and 45 gsm) were able to detect buckling onset only when the buckypaper was positioned far from the impact damage, where the strain field is more uniformly transmitted. In contrast, the 60 gsm buckypaper — with the highest conductivity and sensitivity — detected the onset of buckling both near and far from the damage location. The improved performance at high areal density is also reflected in the higher promptness associated with the displacement at buckling onset compared to the buckling displacement, reported in Table 9. The promptness is evaluated according to Eq. (6)

$$Promptness = 100 \times \frac{Buckling\,Displacement - BucklingOnset}{Buckling\,Displacement} \tag{6}$$

where $Buckling\,Displacement$ is the displacement associated with buckling occurrence (Table 8) while $BucklingOnset$ is the displacement value associated with the first change in normalised electrical resistance that can be used as an indicator of buckling onset.

To conclude the analysis and discussion of the CAI test results, and for the sake of completeness, Tables 10 and 11 show the final

Table 9
Evaluation of buckling onset detection promptness during the CAI test.

Specimen	Buckling displacement [mm]	Buckling onset [mm]	Promptness [%]
BP-20-A	2.09	2.02	9.09
BP-20-B	1.66	–	–
BP-45-A	2.06	1.89	9.71
BP-45-B	2.14	–	–
BP-60-A	2.16	1.50	30.56
BP-60-B	2.11	1.99	5.69

Table 10
Electrical resistance R_f at the end of the CAI test.

Specimen	Channel 1 [Ω]	Channel 2 [Ω]	Channel 3 [Ω]
BP-20-A	1.98	5.66	0.66
BP-20-B	5.35	1.43	1.53
BP-45-A	5.41	0.72	0.73
BP-45-B	2.64	0.71	0.71
BP-60-A	2.86	1.24	1.05
BP-60-B	2.49	0.74	0.79

Table 11
Normalised electrical resistance variation ΔR_n at the end of the CAI test.

Specimen	Channel 1 [Ω]	Channel 2 [Ω]	Channel 3 [Ω]
BP-20-A	2.29	11.99	−1.01
BP-20-B	7.52	7.58	7.79
BP-45-A	83.46	4.12	4.39
BP-45-B	3.00	2.27	2.56
BP-60-A	41.33	153.94	124.21
BP-60-B	23.74	55.17	63.71

electrical resistance values and the final normalised electrical resistance values, respectively, for each channel and specimen. Focusing on Table 10, it can be observed that specimen BP-60-A, impacted on the rear face, exhibits higher electrical resistance values compared to specimen BP-60-B. In contrast, the two specimens manufactured with 45 gsm buckypapers display similar final electrical resistance values, suggesting that the damage location has little to no influence in this case. A similar observation applies to specimens BP-20-A and BP-20-B, for which no clear trend is evident. Moreover, Channel 1 consistently shows higher electrical resistance than Channels 2 and 3 for all specimens, with the exception of specimen BP-20-A, where Channels 1 and 2 exhibit comparable values. This behaviour mirrors the results presented in Table 5 regarding the electrical resistance values prior to the LVI tests, where Channel 1 is generally associated with higher electrical resistance regardless of the specimen. Moving on to the analysis of normalised electrical resistance variation, similar conclusions can be drawn. As shown in Table 11, specimens manufactured with 60 gsm buckypapers exhibit greater ΔR_n variations at the end of the CAI test compared to the other specimens, reflecting their higher sensitivity. Interestingly, in specimens BP-60-A and BP-60-B, Channels 2 and 3 show higher normalised electrical resistance variations than Channel 1. This behaviour contrasts with that of the 45 gsm buckypaper specimens but is consistent with the response of specimens BP-20-A and BP-20-B, except for Channel 3 in BP-20-B. This trend aligns with the results from the tensile tests, where specimens with 60 gsm buckypapers exhibited a combined behaviour characteristic of those observed for the other two surface densities.

The sensitivity of buckypapers to buckling events was found to depend on their areal density. Tables 4 and 5 show that increasing areal density reduces the initial resistance of pristine specimens, indicating the formation of denser and more conductive CNT networks. This improves electromechanical sensitivity by amplifying resistance changes induced by strain or micro-damage. As a result, specimens

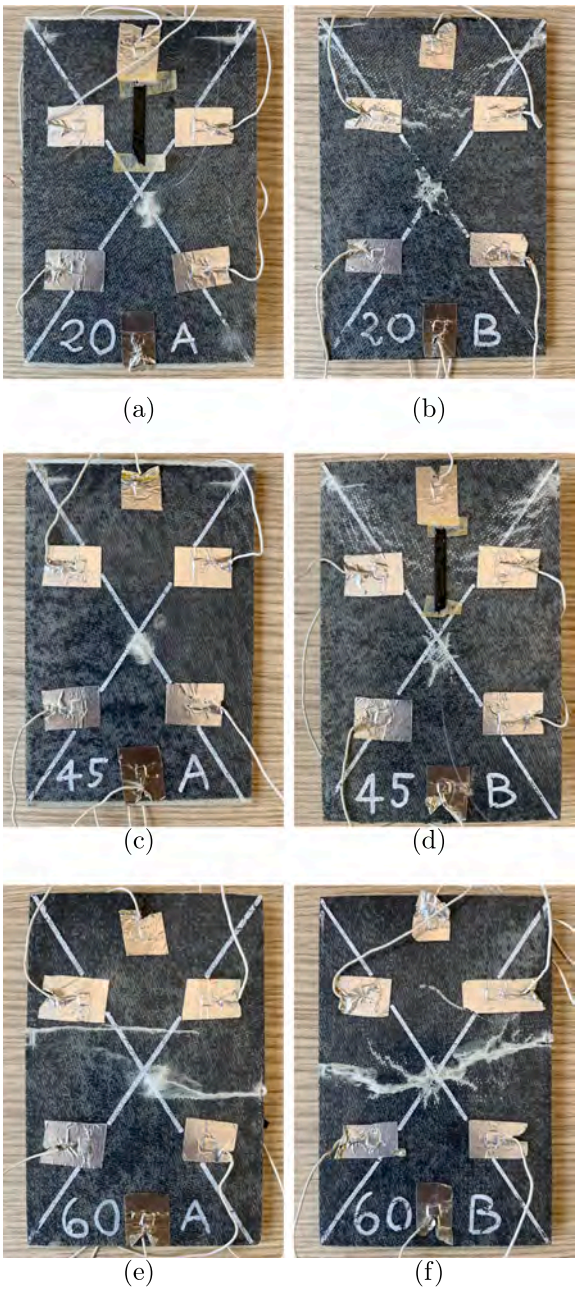

Fig. 27. Specimen pictures after the CAI test: (a) BP-20-A, (b) BP-20-B, (c) BP-45-A, (d) BP-45-B, (e) BP-60-A, and (f) BP-60-B.

with 20 and 45 gsm buckypapers detected buckling onset only when the sensing layer was located far from the impact, while the 60 gsm buckypapers could detect buckling onset both near and far from the damage. This finding confirms the role of CNT content in enhancing detection sensitivity under CAI loading.

5. Conclusions

This work aimed to investigate the applicability of buckypapers for Structural Health Monitoring (SHM) applications. The first objective was to assess the potential influence of buckypapers on the mechanical performance of host materials, which were Glass Fibre Reinforced Plastics (GFRP) plates in this study. Next, an analysis of the electrical measurements acquired from the buckypaper sensor network was performed to observe the electromechanical response under loading and damage conditions to understand how the electrical resistance of buckypapers varies with loads and damage. The final two objectives of this work focused on examining how the electrical response of buckypapers with different CNT content changes under the same testing conditions and how the through-thickness placement of the buckypaper affects the sensing capability.

To accomplish these goals, two types of specimens with different geometries were fabricated: Type-1 specimens for tensile tests and Type-2 specimens for Low-Velocity Impact (LVI) and CAI tests. Type-1 specimens were manufactured both without buckypapers (pristine GFRPs) and with buckypapers with three different CNT contents to observe the effect of buckypaper addition and CNT content on mechanical strength. Two Type-2 specimens were made for each buckypaper CNT content. The electromechanical response of buckypapers was analysed for both Type-1 and Type-2 specimens. Type-1 specimens were analysed under tensile tests, while Type-2 specimens underwent electrical measurements during impact and post-impact compression tests because these conditions induce out-of-plane damage to which composite materials, such as GFRPs, are susceptible. The impacts were performed on the face of the specimen, either close or far from the buckypaper, to observe the influence of buckypaper placement on sensing capabilities. Finally, the Compression After Impact (CAI) test aimed to prove the ability of the buckypaper-based sensor network to continue sensing after the occurrence of damage. This is mandatory for SHM purposes since a sensor network should be able to monitor after sustaining damage.

The experimental campaign was conducted according to ASTM standards, with tests performed under controlled and qualified conditions to ensure the accuracy of the investigation's outcomes. The key findings of this study are as follows:

- It is possible to use buckypapers without compromising the mechanical performance of the host material. This finding is supported by the tensile test results, which also showed no significant effect of buckypaper CNT content on mechanical properties, as all specimens exhibited a UTS of around 286 MPa. This is a crucial outcome because it allows the use of the highest possible conductivity, i.e., the highest CNT content. This is desirable for monitoring purposes, as increased conductivity enhances sensitivity. In addition, this is a significant advantage of buckypapers over CNT dispersion in the matrix, as they prevent the formation of agglomerates. Therefore, not only is it possible to use buckypapers for monitoring without compromising the mechanical performance of components, but it is also feasible to use the highest conductivity available and achieve the highest sensitivity.
- The tensile test highlighted the ability of buckypapers to detect microdamage formation around 50 MPa. According to the literature, this stress value is associated with the fatigue strength of composite materials such as GFRPs. The buckypaper's response to micro-damage varies with CNT content. 20 gsm buckypapers showed a step resistance increment after an initial period of stable resistance. 45 gsm buckypapers exhibited a linear normalised resistance variation with strain in the region where 20 gsm buckypapers showed step resistance increments. This can be attributed to the higher conductivity, which allows the sensing of the entire damage formation process. Finally, 60 gsm buckypapers showed an initial decrease in electrical resistance due to the Poisson's effect, followed by a step increment similar to what was described for 20 gsm buckypapers.
- Low-Velocity Impact tests revealed that neither the buckypaper CNT content nor the proximity to the impact location influenced the energy absorbed by the specimens. Four zones were identified: (i) an initial pre-impact region with no load and no ΔR_n variation, (ii) a zone where the impact event was monitored with sharp variations in load and electrical resistances, (iii) a first post-impact region associated with oscillations of both the impactor and specimens, and (iv) a second post-impact zone in which the

oscillations were dampened, and a permanent shift in electrical resistance occurred, which is associated with the presence of a damage. Buckypapers closer to the impact location exhibited higher ΔR_n variations since they are more affected by the impact damage. It was found that the through-thickness placement of the buckypaper does not significantly affect its impact monitoring capabilities, although damage mechanism indicators were more easily identifiable in specimens impacted on the rear side. However, associating electrical resistance variation with damage mechanisms is more complex when using buckypapers compared to CNT dispersed in the composite matrix. This is because buckypapers can only sense at a specific location in the thickness of the specimen and not across the thickness.

- CAI tests highlighted that buckypapers placed far from the damage site were able to provide indicators of buckling onset, regardless of buckypaper conductivity. Only 60 gsm buckypaper was able to do the same when placed close to the impact location. The indicators were identified as slope changes and step increments in ΔR_n variation. Slight differences in the behaviour of 60 gsm buckypapers were identified depending on the distance of the buckypaper from the damage location. However, all the specimens showed a change in electrical resistance behaviour when the compressive load began to vary linearly with the displacement, due to the more uniform compressive field induced in the specimens. It was still possible to monitor the specimens using the buckypaper-based sensor network that was previously damaged during the LVI tests.

In summary, the experimental tests demonstrated the applicability of buckypapers as a sensor network for Structural Health Monitoring applications when embedded in non-conductive composites. Specifically, the best monitoring performance is achieved when using buckypapers with the highest conductivity, i.e., 60 gsm buckypapers. Variations in buckypaper conductivity can be used to monitor strain and damage, including sudden events like impacts.

The great advantage of using buckypapers instead of CNT dispersed in the matrix is the ability to achieve the highest possible conductivity, which results in the best sensitivity for the sensor network, without compromising mechanical performance and avoiding CNT agglomeration. Additionally, buckypaper-based sensor networks can monitor the entire structure without the need to select specific locations for external sensors.

While buckypapers can detect damage, a direct correlation between electrical resistance variations and damage diagnosis, such as localisation and severity assessment, and mechanisms, requires further investigation. Therefore, future studies will incorporate non-destructive imaging (e.g., X-ray tomography) and SEM analyses to provide direct evidence of interlaminar damage evolution and further validate the electromechanical measurements. Additional effort will be devoted to utilising the damage detection capability of buckypapers to trigger other monitoring systems for damage diagnosis and to developing methods and algorithms for buckypaper-based damage assessment.

CRediT authorship contribution statement

Lucio Pinello: Writing – review & editing, Writing – original draft, Visualization, Formal analysis. **Patel Bhavik:** Investigation, Formal analysis, Data curation. **Marco Giglio:** Supervision, Resources. **Claudio Sbarufatti:** Writing – review & editing, Supervision, Project administration, Methodology, Funding acquisition, Conceptualization.

Declaration of competing interest

The authors declare that they have no known competing financial interests or personal relationships that could have appeared to influence the work reported in this paper.

Data availability

Data will be made available on request.

References

[1] Wood L. Global composites industry overview 2018–2023 - increasing demand for lightweight materials in the aerospace & defense and automotive industry. 2018, available online: https://www.prnewswire.com/news-releases/global-composites-industry-overview-2018-2023—increasing-demand-for-lightweight-materials-in-the-aerospace–defense-and-automotive-industry-300673139.html.

[2] Tuttle ME, Brinson HF. Resistance-foil strain-gage technology as applied to composite materials. Exp Mech 1984;24(1):54–65.

[3] López-Higuera JM, Cobo LR, Incera AQ, Cobo A. Fiber optic sensors in structural health monitoring. J Lightwave Technol 2011;29(4):587–608.

[4] Bremer K, Wollweber M, Weigand F, Rahlves M, Kuhne M, Helbig R, Roth B. Fibre optic sensors for the structural health monitoring of building structures. Procedia Technol 2016;26:524–9. http://dx.doi.org/10.1016/j.protcy.2016.08.065, 3rd International Conference on System-Integrated Intelligence: New Challenges for Product and Production Engineering.

[5] Tian J, Wu X, Tan X, Zuo Y, Zheng Y, Yuan J, Wang W-W, Wei L, Zhang W. Feasibility study of smart functional strain-hardening cementitious composites: Self-sensing model and experimental performance. Constr Build Mater 2024;436:136850. http://dx.doi.org/10.1016/j.conbuildmat.2024.136850.

[6] Paipetis A, Kostopoulos V. In: carbon nanotube enhanced aerospace composite materials: a new generation of multifunctional hybrid structural composites, vol. 188, Springer Science & Business Media; 2012, https://link.springer.com/content/pdf/10.1007/978-94-007-4246-8.pdf.

[7] Tallman TN, Smyl DJ. Structural health and condition monitoring via electrical impedance tomography in self-sensing materials: a review. Smart Mater Struct 2020;29(12):123001. http://dx.doi.org/10.1088/1361-665X/abb352.

[8] Chung D. Carbon materials for structural self-sensing, electromagnetic shielding and thermal interfacing. Carbon 2012;50(9):3342–53. http://dx.doi.org/10.1016/j.carbon.2012.01.031, festschrift dedicated to Peter A. Thrower, Editor-in-Chief, 1972-2012.

[9] Hu N, Karube Y, Arai M, Watanabe T, Yan C, Li Y, Liu Y, Fukunaga H. Investigation on sensitivity of a polymer/carbon nanotube composite strain sensor. Carbon 2010;48(3):680–7. http://dx.doi.org/10.1016/j.carbon.2009.10.012.

[10] Ku-Herrera J, Avlies F, Seidel G. Cyclic tension and compression piezoresistivity of carbon nanotube/vinyl ester composites in the elastic and plastic regimes. Carbon 2012;50(7):2592–8. http://dx.doi.org/10.1016/j.carbon.2012.02.018.

[11] Piegney A, Laurent C, Flahaut E, Basca R, Rousset A. Specific surface area of carbon nanotubes and bundles of carbon nanotubes. Carbon 2001;39(4):507–14. http://dx.doi.org/10.1016/S0008-6223(00)00155-X.

[12] Baltopoulos A, Polydorides N, Pambaguian L, Vavouliotis A, Kostopoulos V. Exploiting carbon nanotube networks for damage assessment of fiber reinforced composites. Compos Part B: Eng 2015;76:149–58. http://dx.doi.org/10.1016/j.compositesb.2015.02.022.

[13] Rawat P, Behera R, Singh K. Tensile behavior of three phased glass/epoxy laminate embedded with mwcnts: An experimental approach. Mater Today: Proc - Int Conf Emerg Trends Mater Manuf Eng (IMME17) 2018;5(2, Part 2):8176–83. http://dx.doi.org/10.1016/j.matpr.2017.11.506.

[14] Martin C, Sandler J, Windle A, Schwarz M, Baubofer W, Schulte K, Shaffer M. Electric field-induced aligned multi-wall carbon nanotube networks in epoxy composites. Polymer 2005;46(3):877–86. http://dx.doi.org/10.1016/j.polymer.2004.11.081.

[15] Qu B, Zhou D, Wang R, Wu L, Cheng X. Enhancement of mechanical properties of buckypapers/polyethylene composites by microwave irradiation. Compos Sci Technol 2018;164:313–8. http://dx.doi.org/10.1016/j.compscitech.2018.06.002.

[16] Vertuccio L, Guadagno L, Spinelli G, Lamberti P, Tucci V, Russo S. Piezoresistive properties of resin reinforced with carbon nanotubes for health-monitoring of aircraft primary structures. Compos Part B: Eng 2016;107:192–202. http://dx.doi.org/10.1016/j.compositesb.2016.09.061.

[17] Yan C, Njuguna M, Hu N, Bell J, Yarlagadda P. Sandwiched carbon nanotube film as strain sensor. Compos Part B: Eng 2012;43(6):2711–7. http://dx.doi.org/10.1016/j.compositesb.2012.04.022.

[18] Obitayo W, Liu T. A review: Carbon nanotube-based piezoresistive strain sensor. J Sensors 2012. http://dx.doi.org/10.1155/2012/652438.

[19] Pinello L, Sánchez-Romate XXF, Vescovini A, Cinquemani S, Scaccabarozzi D, Libonati F, Suárez AJ, Ureña A, Sbarufatti C. In-situ monitoring of impact dynamics, indentation, and compression after impact (cai) on cnt-doped gfrp panels by means of electrical monitoring. Struct Heal Monit 2025.

[20] Esmaeili A, Sbarufatti C, Ma D, Manes A, Jiménez-Suárez A, Ureña A, Dellasega D, Hamouda A. Strain and crack growth sensing capability of swcnt reinforced epoxy in tensile and mode i fracture tests. Compos Sci Technol 2020;186:107918. http://dx.doi.org/10.1016/j.compscitech.2019.107918.

[21] Xiaoqiang W, Shaowei L, Keming M, Xuhai X, Haijun Z, Meijuan X. Tensile strain sensing of buckypaper and buckypaper composites. Mater Des 2015;88:414–9. http://dx.doi.org/10.1016/j.matdes.2015.09.035.

[22] Neerukatti R, Datta S, Chattopadhyay A. Buckypaper embedded self-sensing composite for real-time fatigue damage diagnosis and prognosis. Carbon 2018;139:353–60. http://dx.doi.org/10.1016/j.carbon.2018.06.059.

[23] Dumstorff G, Lang W. Strain gauges — volume embedding vs. surface application. In: SENSORS, 2014. IEEE; 2014, p. 1292–4. http://dx.doi.org/10.1109/ICSENS.2014.6985247.

[24] Aly K, Li A, Bradford P. Strain sensing in composites using aligned carbon nanotube sheets embedded in the interlaminar region. Compos Part A: Appl Sci Manuf 2016;90:536–48. http://dx.doi.org/10.1016/j.compositesa.2016.08.003.

[25] Kang I, Schulz M, Kim J, Shanov V, Shi D. A carbon nanotube strain sensor for structural health monitoring. Smart Mater Struct 2006;15:737. http://dx.doi.org/10.1088/0964-1726/15/3/009.

[26] Zhang Z, Wei H, Liu Y, Leng J. Self-sensing properties of smart composite based on embedded buckypaper layer. Struct Heal Monit 2015;14(2):127–36. http://dx.doi.org/10.1177/1475921714568405.

[27] Vescovini A, Cruz JA, Ma D, Colombo C, Salerno A, Bianchi O, Amico SC, Manes A. Experimental investigation on low-velocity impact behavior of glass, kevlar, and hybrid composites with an elastomeric polyurethane matrix. Compos Part C: Open Access 2024;13:100426. http://dx.doi.org/10.1016/j.jcomc.2023.100426.

[28] Stephen C, Shivamurthy B, Mohan M, Mourad A-HI, Selvam R, Thimmappa B. Low velocity impact behavior of fabric reinforced polymer composites–a review. Eng Sci 2022;18(8):75–97.

[29] Dogan A, Arikan V. Low-velocity impact response of e-glass reinforced thermoset and thermoplastic based sandwich composites. Compos Part B: Eng 2017;127:63–9. http://dx.doi.org/10.1016/j.compositesb.2017.06.027.

[30] Lu S, Du K, Wang X, Tian C, Chen D, Ma K, Xu T. Real-time monitoring of low-velocity impact damage for composite structures with the omnidirection carbon nanotubes' buckypaper sensors. Struct Heal Monit 2019;18(2):454–65. http://dx.doi.org/10.1177/1475921718757937.

[31] Sánchez-Romate X, Artigas J, Jiménez-Suárez A, Sánchez M, Güemes A, Ureña A. Critical parameters of carbon nanotube reinforced composites for structural health monitoring applications: Empirical results versus theoretical predictions. Compos Sci Technol 2019;171:44–53. http://dx.doi.org/10.1016/j.compscitech.2018.12.010.

[32] Li C, Thostenson E, Chou T-W. Dominant role of tunneling resistance in the electrical conductivity of carbon nanotube–based composites. Appl Phys Lett 2007;91(22):223114. http://dx.doi.org/10.1063/1.2819690.

[33] Hu N, Karube Y, Yan C, Masuda Z, Fukunaga H. Tunneling effect in a polymer/carbon nanotube nanocomposite strain sensor. Acta Mater 2008;56(13):2929–36. http://dx.doi.org/10.1016/j.actamat.2008.02.030.

[34] Gong S, Zhu ZH, Haddad EI. Modeling electrical conductivity of nanocomposites by considering carbon nanotube deformation at nanotube junctions. J Appl Phys 2013;114(7):074303. http://dx.doi.org/10.1063/1.4818478.

[35] Li H, Lu W, Li J, Bai X, Gu C. Multichannel ballistic transport in multiwall carbon nanotubes. Phys Rev Lett 2005;95:086601. http://dx.doi.org/10.1103/PhysRevLett.95.086601.

[36] De Vivo B, Lamberti P, Spinelli G, Tucci V, Vertuccio L, Vittoria V. Simulation and experimental characterization of polymer/carbon nanotubes composites for strain sensor applications. J Appl Phys 2014;116(5):054307. http://dx.doi.org/10.1063/1.4892098.

[37] Gao L, Chou T, Thostenson E, Zhang Z, Coulaud M. In situ sensing of impact damage in epoxy/glass fiber composites using percolating carbon nanotube networks. Carbon 2011;49(10):3382–5. http://dx.doi.org/10.1016/j.carbon.2011.04.003.

[38] Aly K, Bradford P. Real-time impact damage sensing and localization in composites through embedded aligned carbon nanotube sheets. Compos Part B: Eng 2019;162:522–31. http://dx.doi.org/10.1016/j.compositesb.2018.12.104.

[39] Uribe-Riestra G, Ocampo-Bello J, Gamboa F, Mendoza-Santoyo F, Pérez-López C, Franco-Urquiza E, Preud'homme M, Castillo-Atoche A, Avilès, F. Influence of electrode configuration on impact damage evaluation of self-sensing hierarchical composites. J Intell Mater Syst Struct 2020;31(11):1416–29. http://dx.doi.org/10.1177/1045389X20919979.

[40] Sanchez-Romate X, Sbarufatti C, Scaccabarozzi D, Cinquemani S, Jimenez-Suarez A, Guemes A, Ureña A and. Monitoring of impact dynamics on carbon nanotube multiscale glass fiber composites by means of electrical measurements. In: Kundu T, editor. Health monitoring of structural and biological systems 2017 10170, international society for optics and photonics. SPIE; 2017, p. 101703A. http://dx.doi.org/10.1117/12.2259976.

[41] Sbaruffatti C, Simon P, Cinquemani S, Scaccabarozzi D. Impact analysis of fiber-reinforced composites by means of carbon nanotubes. In: Erturk A, editor. Active and passive smart structures and integrated systems XII, 10595, international society for optics and photonics. SPIE; 2018, p. 1059538. http://dx.doi.org/10.1117/12.2292641.

[42] Al-Bahrani M, Cree A. A simple criterion to evaluate the degree of damage in composite materials after sudden impact loads by exploiting the mwcnts piezoresistive property. Carbon 2019;150:505–17. http://dx.doi.org/10.1016/j.carbon.2019.05.053.

[43] Isaac-Medina B, Alonzo-García A, Avilés F. Electrical self-sensing of impact damage in multiscale hierarchical composites with tailored location of carbon nanotube networks. Struct Heal Monit 2019;18(3):806–18. http://dx.doi.org/10.1177/1475921718776198.

[44] Uribe-Riestra G, Ayuso-Faber P, Rivero-Ayala M, Cauich-Cupul J, Gamboa F, Avilés F. Structural health monitoring of carbon nanotube-modified glass fiber-reinforced polymer composites by electrical resistance measurements and digital image correlation. Struct Heal Monit 2024;23(1):555–67. http://dx.doi.org/10.1177/14759217231173439.

[45] Naghashpour A, Van Hoa S. A technique for real-time detecting, locating, and quantifying damage in large polymer composite structures made of carbon fibers and carbon nanotube networks. Struct Heal Monit 2015;14(1):35–45. http://dx.doi.org/10.1177/1475921714546063.

[46] NanoTechLabs. Buckypaper mf series. 2018, available online: https://www.nanotechlabs.com/pdfs/New%20High%20Conductivity%20MWNT%20Blend%20Buckypaper%2045%20gsm.pdf.

[47] ASTM. Astm d3039/d3039m-08 standard test method for tensile properties of polymer matrix composite materials. 2008.

[48] ASTM. Astm d7136/d7136m-15 standard test method for measuring the damage resistance of a fiber-reinforced polymer matrix composite to a drop-weight impact event. 2020.

[49] ASTM. Astm d7137/d7137m-12 standard test method for compressive residual strength properties of damaged polymer matrix composite. 2017.

[50] Naghashpour A, Van Hoa S. Coupled health monitoring system for cnt-doped self-sensing composites. Carbon 2020;166:193–204. http://dx.doi.org/10.1016/j.carbon.2020.04.060.

[51] Colombo C, Libonati F, Vergani L. Fatigue damage in gfrp. Int J Struct Integr 2012;3(14):424–40. http://dx.doi.org/10.1108/17579861211281218.

[52] Libonati F, Vergani L. Damage assessment of composite materials by means of thermographic analyses. Compos Part B: Eng 2013;50:82–90. http://dx.doi.org/10.1016/j.compositesb.2013.01.012.

[53] Colombo C, Libonati F, Pezzani F, Salerno A, Vergani L. Fatigue behaviour of a gfrp laminate by thermographic measurements. Procedia Eng 2011;10:3518–27. http://dx.doi.org/10.1016/j.proeng.2011.04.579.

[54] Khan SU, Kim J-K. Improved interlaminar shear properties of multiscale carbon fiber composites with bucky paper interleaves made from carbon nanofibers. Carbon 2012;50(14):5265–77. http://dx.doi.org/10.1016/j.carbon.2012.07.011.

[55] Wu Y, Cheng X, Chen S, Qu B, Wang R, Zhuo D, Wu L. In situ formation of a carbon nanotube buckypaper for improving the interlaminar properties of carbon fiber composites. Mater Des 2021;202:109535. http://dx.doi.org/10.1016/j.matdes.2021.109535.

[56] Zhang H, Bilotti E, Pejis T. The use of carbon nanotubes for damage sensing and structural health monitoring in laminated composites: a review. Nanocomposites 2015;1(4):167–84. http://dx.doi.org/10.1080/20550324.2015.1113639.

[57] Salvetti M, Sbarufatti C, Gilioli A, Dziendzikowski M, Dragan K, Manes A, Giglio M. On the mechanical response of cfrp composite with embedded optical fibre when subjected to low velocity impact and cai tests. Compos Struct 2017;179:21–34. http://dx.doi.org/10.1016/j.compstruct.2017.07.063.

[58] Ouyang T, Sun W, Bao R, Tan R. Effects of matrix cracks on delamination of composite laminates subjected to low-velocity impact. Compos Struct 2021;262:113354. http://dx.doi.org/10.1016/j.compstruct.2020.113354.

[59] Ghelli D, Minak G. Low velocity impact and compression after impact tests on thin carbon/epoxy laminates. Compos Part B: Eng 2011;42(7):2067–79. http://dx.doi.org/10.1016/j.compositesb.2011.04.017.

[60] Sun X, Hallet S. Barely visible impact damage in scaled composite laminates: Experiments and numerical simulations. Int J Impact Eng 2017;109:178–95. http://dx.doi.org/10.1016/j.ijimpeng.2017.06.008.